Energy cascade with small-scale thermalization, counterflow metastability, and anomalous velocity of vortex rings in Fourier-truncated Gross-Pitaevskii equation

Giorgio Krstulovic and Marc Brachet

Laboratoire de Physique Statistique de l'Ecole Normale Supérieure, associé au CNRS et aux Universités Paris VI et VII, 24 Rue Lhomond, F-75231 Paris, France

(Received 30 September 2010; revised manuscript received 12 February 2011; published 16 June 2011)

The statistical equilibria of the (conservative) dynamics of the Gross-Pitaevskii equation (GPE) with a finite range of spatial Fourier modes are characterized using a new algorithm, based on a stochastically forced Ginzburg-Landau equation (SGLE), that directly generates grand-canonical distributions. The SGLE-generated distributions are validated against finite-temperature GPE-thermalized states and exact (low-temperature) results obtained by steepest descent on the (grand-canonical) partition function. A standard finite-temperature second-order λ transition is exhibited. A mechanism of GPE thermalization through a direct cascade of energy is found using initial conditions with mass and energy distributed at large scales. A long transient with partial thermalization at small scales is observed before the system reaches equilibrium. Vortices are shown to disappear as a prelude to final thermalization and their annihilation is related to the contraction of vortex rings due to mutual friction. Increasing the amount of dispersion at the truncation wave number is shown to slow thermalization and vortex annihilation. A bottleneck that produces spontaneous effective self-truncation with partial thermalization is characterized in the limit of large dispersive effects. Metastable counterflow states, with nonzero values of momentum, are generated using the SGLE algorithm. Spontaneous nucleation of the vortex ring is observed and the corresponding Arrhenius law is characterized. Dynamical counterflow effects on vortex evolution are investigated using two exact solutions of the GPE: traveling vortex rings and a motionless crystal-like lattice of vortex lines. Longitudinal effects are produced and measured on the crystal lattice. A dilatation of vortex rings is obtained for counterflows larger than their translational velocity. The vortex ring translational velocity has a dependence on temperature that is an order of magnitude above that of the crystal lattice, an effect that is related to the presence of finite-amplitude Kelvin waves. This anomalous vortex ring velocity is quantitatively reproduced by assuming equipartition of energy of the Kelvin waves. Orders of magnitude are given for the predicted effects in weakly interacting Bose-Einstein condensates and superfluid ^{4}He.

DOI: 10.1103/PhysRevE.83.066311 PACS number(s): 47.27.−i, 03.75.Kk, 05.30.Jp, 47.37.+q

I. INTRODUCTION

Finite-temperature superfluids are typically described as a mixture of two interpenetrating fluids [1]. At low temperatures the normal fluid can be neglected and Landau's two-fluids model reduces to the Euler equation for an ideal fluid that is irrotational except on (singular) vortex lines around which the circulation of the velocity is quantized. At finite temperature, when both normal fluid and superfluid vortices are present (e.g., in the counterflow produced by a heat current) their interaction, called "mutual friction," must also be accounted for [2].

In the low-temperature regime the Gross-Pitaevskii equation (GPE) (also called the nonlinear Schrödinger equation) is an alternative description of superfluids and Bose-Einstein condensates (BEC) [3]. The GPE is a partial differential equation (PDE) for a complex wave field that is related to the superflow's density and velocity by Madelung's transformation [4]. The (nonsingular) nodal lines of the complex wave field correspond to the quantum vortices that appear naturally in this model with the correct amount of velocity circulation. Just as the incompressible Euler equation, the GPE dynamics is known to produce [5–8] an energy cascade that leads to a Kolmogorov regime with an energy spectrum scaling as $E(k) \sim k^{-5/3}$. This Kolmogorov regime was also experimentally observed in low-temperature helium [9,10]. In this experimental context, let us remark that so much progress has been made that it is now possible to visualize superfluid vortices both in the low-temperature regime and in the presence of counterflow by following the trajectories of solid hydrogen tracers in helium [11,12].

Several different theories of finite-temperature effects in BEC have been proposed and, at the moment, there is no consensus on the best model [3]. In one approach it has been suggested that, beyond its good description of the low-temperature regime, the GPE should also be able to describe the classical equilibrium aspects of a finite-temperature homogeneous system of ultracold gases, provided that that a projection (or truncation) on a finite number of Fourier modes is performed [3,13]. Another approach to finite temperatures is the Zaremba-Nikuni-Griffin (ZNG) theory [14] which couples the GPE with a Boltzmann-like equation for the thermal cloud of noncondensed particles. The ZNG theory is known to well describe the observed finite-temperature decay of solitons [15]. It also predicts vortex motion in agreement with the standard phenomenology [16]. In the truncated GPE model the small-scales modes are in thermal equilibrium. They play the role of the Boltzmann sector of the ZNG, somewhat like the (fast) thermalized degrees of freedom do in a standard molecular dynamics simulation. The present paper is devoted to the truncated GPE approach.

Classical truncated systems, which are similar to the truncated GPE, have a long history in the context of fluid mechanics. Indeed, if the (conservative) Euler equation is spectrally truncated, by keeping only a finite number of

spatial Fourier harmonics, it is well known that it admits absolute equilibrium solutions with Gaussian statistics and equipartition of kinetic energy among all Fourier modes [17–20]. Recently, a series of papers focused on the dynamics of convergence of the truncated Euler equation toward the absolute equilibrium. It was found that (long-lasting) transients are obtained that are able to mimic (irreversible) viscous effects because of the presence of a "gas" of partially thermalized high-wave-number Fourier modes that generate (pseudo-) dissipative effects [21–26].

The main goal of the present paper is to obtain and study finite-temperature dissipative and counterflow effects by extending to the Fourier-truncated GPE the dynamical results that were obtained in the framework of the truncated Euler equation. We now give a short review of what is already known about the truncated GPE dynamics.

The Fourier truncated Gross-Pitaevskii equation was first introduced in the context of Bose condensation by Davis *et al*. [13] as a description of the classical modes of a finite-temperature partially condensed homogeneous Bose gas. They considered random initial data defined in Fourier space by modes with constant modulus and random phases up to some maximum wave number (determined by the energy). They found that the numerical evolution of the truncated Gross-Pitaevskii equation reached (microcanonical) equilibrium and that a condensation transition of the equilibrium was obtained when the initial energy was varied.

The same condensation transition was later studied by Connaughton *et al*. [27] and interpreted as a condensation of classical nonlinear waves. Using a modified wave turbulence theory with ultraviolet cutoff, they argued that the transition to condensation should be subcritical. They found their theory in quantitative agreement with numerical integration of the GPE, using the same stochastic initial conditions than those of Ref. [13]. However, the authors later argued that, as weak turbulence theory is expected to break down near the transition to condensation, the subcritical nature of the transition predicted by their theory was not physical [28].

Berloff and Svistunov [29], starting from periodic initial conditions similar to those of Davis *et al*. [13], used a finite-difference scheme (exactly conserving energy and particle number) to characterized the dynamical scenario of the relaxation toward equilibrium. Using the same finite-difference scheme, Berloff and Youd [30] then studied the dissipative dynamics of superfluid vortices at nonzero temperatures and observed a contraction of the vortex rings that followed a universal decay law.

Our main results are as follows. The classical absolute equilibrium of ideal fluids when generalized to GPE superfluids describes a standard [31,32] second-order phase transition. Long transients with an energy cascade and partial small-scale thermalization are present in the relaxation dynamics. Dynamical counterflow effects on vortex evolution are naturally present in the system and the vortex ring has anomalous velocities caused by thermally excited Kelvin waves.

The paper is organized as follows: Section II is devoted to the basic theoretical background that is needed to account for the dynamics and thermalization of the Fourier truncated GPE. In Sec. III, the thermodynamic equilibrium is explored. The microcanonical and grand-canonical distributions are numerically shown to be equivalent. Exact analytical expressions for the low-temperature thermodynamic functions are obtained. A standard second-order λ phase transition is exhibited at finite-temperature using the SGLE-generated grand-canonical states.

In Sec. IV, the direct energy cascade is considered as a new mechanism for GPE thermalization. Using initial data with mass and energy distributed at large scales, a long transient with partial thermalization at small scales is characterized. Vortex annihilation is observed to take place and is related to mutual friction effects. A bottleneck producing spontaneous self-truncation with partial thermalization and a time-evolving effective truncation wave number is characterized in the limit of large dispersive effects at the maximum wave number of the simulation.

In Sec. V, the new SGLE algorithm is used to generate counterflow states, with nonzero values of momentum, that are shown to be metastable under SGLE evolution. The spontaneous nucleation of vortex ring and the corresponding Arrhenius law are characterized. Dynamical counterflow effects are investigated using vortex rings and straight vortex lines arranged in crystal-like patterns. An anomalous translational velocity of the vortex ring is exhibited and is quantitatively related to the effect of thermally excited finite-amplitude Kelvin waves. Orders of magnitude are estimated for the corresponding effects in weakly interacting Bose-Einstein condensates and superfluid ^{4}He.

Section VI is our conclusion. The numerical methods and low-temperature thermodynamic functions are described in an Appendix.

II. THEORETICAL BACKGROUND

This section deals with basic facts needed to understand the dynamics and thermalization of the Fourier truncated GPE. We first recall in Sec. II A 1 the (untruncated) GPE dynamics and its associated conserved quantities and the corresponding spectra; this material can be skipped by the reader already familiar with the GPE model of superflow [4,6]. The Fourier truncated GPE, its thermodynamical limit and the different statistical ensembles are then defined.

The thermodynamics of the truncated system is introduced in Sec. II B using the microcanonical distribution. The canonical and grand-canonical distributions are also used as they allow to directly label the equilibrium states by temperature and particle numbers. A stochastically forced Ginzburg-Landau equation (SGLE) is considered in Sec. II C and shown to define a new algorithm that directly generates the grand-canonical distributions.

A. Galerkin-truncated Gross-Pitaevskii equation

1. Conservation laws and Galilean invariance of the GPE

Superfluids and Bose-Einstein condensates [3,33] can be described at low temperature by the Gross-Pitaevskii equation (GPE) that is a partial differential equation (PDE) for the complex field ψ that reads

$$i\hbar\frac{\partial\psi}{\partial t} = -\frac{\hbar^2}{2m}\nabla^2\psi + g|\psi|^2\psi, \tag{1}$$

where $|\psi|^2$ is the number of particles per unit volume, m is the mass of the condensed particles, and $g = \frac{4\pi\tilde{a}\hbar^2}{m}$, with $\tilde{a}$ the s-wave scattering length. This equation conserves the Hamiltonian H, the total number of particles N, and the momentum $\mathbf{P}$ defined in volume V by

$$H = \int_V d^3x \left(\frac{\hbar^2}{2m}|\nabla\psi|^2 + \frac{g}{2}|\psi|^4\right) \tag{2}$$

$$N = \int_V |\psi|^2 d^3x \tag{3}$$

$$\mathbf{P} = \int_V \frac{i\hbar}{2}(\psi\nabla\overline{\psi} - \overline{\psi}\nabla\psi) d^3x. \tag{4}$$

It will be useful for the next sections to explicitly write the conservation law of the momentum $\partial_t \frac{i\hbar}{2}(\psi\partial_j\overline{\psi} - \overline{\psi}\partial_j\psi) + \partial_k\Pi_{kj} = 0$, where the momentum flux tensor Π_{kj} is defined, following Ref. [6], as

$$\Pi_{kj} = \frac{\hbar^2}{2m}(\partial_k\overline{\psi}\partial_j\psi + \partial_k\psi\partial_j\overline{\psi}) + \delta_{kj}\left(\frac{g}{2}|\psi|^4 - \frac{\hbar^2}{4m}\nabla^2|\psi|^2\right). \tag{5}$$

It is well known that the GPE (1) can be mapped into hydrodynamics equations of motion for a compressible irrotational fluids using the Madelung transformation defined by

$$\psi(\mathbf{x},t) = \sqrt{\frac{\rho(\mathbf{x},t)}{m}}\exp\left[i\frac{m}{\hbar}\phi(\mathbf{x},t)\right], \tag{6}$$

where $\rho(\mathbf{x},t)$ is the fluid density and $\phi(\mathbf{x},t)$ is the velocity potential such that $\mathbf{v} = \nabla\phi$. The Madelung transformation (6) is singular on the zeros of ψ. As two conditions are required (both real and imaginary part of ψ must vanish) these singularities generally take place on points in two dimensions and on curves in three dimensions. The Onsager-Feynman quantum of velocity circulation around vortex lines $\psi = 0$ is given by h/m.

When Eq. (1) is linearized around a constant $\psi = A_0$, the sound velocity is given by $c = \sqrt{g|A_0|^2/m}$ with dispersive effects taking place for length scales smaller than the coherence length defined by

$$\xi = \sqrt{\hbar^2/2m|A_0|^2 g}. \tag{7}$$

ξ is also the length scale of the vortex core [3,6].

Following Ref. [5] we define the total energy per unit volume $e_{\rm tot} = (H - \mu N)/V - \mu^2/2g$, where μ is the chemical potential (see Sec. II B). Using the hydrodynamical variables, $e_{\rm tot}$ can be written as the sum of three parts (the kinetic energy $e_{\rm kin}$, the internal energy $e_{\rm int}$, and the quantum energy e_q) defined by

$$e_{\rm kin} = \frac{1}{V}\int d^3x \frac{1}{2}(\sqrt{\rho}\mathbf{v})^2 \tag{8}$$

$$e_{\rm int} = \frac{1}{V}\int d^3x \frac{g}{2m^2}\left(\rho - \frac{\mu m}{g}\right)^2 \tag{9}$$

$$e_q = \frac{1}{V}\int d^3x \frac{\hbar^2}{2m^2}(\nabla\sqrt{\rho})^2. \tag{10}$$

Using Parseval's theorem, one can define corresponding energy spectra, e.g., the kinetic energy spectrum $e_{\rm kin}(k)$ is defined as the sum over the angles

$$e_{\rm kin}(k) = \int \left|\frac{1}{V}\int d^3r e^{i\mathbf{r}\cdot\mathbf{k}}\sqrt{\rho}\mathbf{v}\right|^2 k^2 d\Omega_k, \tag{11}$$

where $d\Omega_k$ is the solid angle element on the sphere. The energy $e_{\rm kin}$ can be further decomposed into a compressible part $e^c_{\rm kin}$ and an incompressible part $e^i_{\rm kin}$ by making use of the relation $\sqrt{\rho}\mathbf{v} = (\sqrt{\rho}\mathbf{v})^c + (\sqrt{\rho}\mathbf{v})^i$ with $\nabla\cdot(\sqrt{\rho}\mathbf{v})^i = 0$ (see Ref. [6] for details).

Finally note that the GPE (1) is invariant under the Galilean transformation

$$\psi'(\mathbf{x},t) = \psi(\mathbf{x} - \mathbf{v}_{\rm G}t, t)\exp\left\{\frac{im}{\hbar}\left[\mathbf{v}_{\rm G}\cdot\mathbf{x} - \frac{1}{2}v_{\rm G}^2 t\right]\right\}. \tag{12}$$

Under this transformation Eqs. (2)–(4) transform as

$$H' = \tfrac{1}{2}mNv_{\rm G}^2 + \mathbf{P}\cdot\mathbf{v}_{\rm G} + H \tag{13}$$

$$N' = N \tag{14}$$

$$\mathbf{P}' = mN\mathbf{v}_{\rm G} + \mathbf{P}. \tag{15}$$

2. *Definition of the Fourier truncated GPE*

For a periodical 3D system of volume V the Fourier truncated GPE is defined by performing a Galerkin truncation that consists in keeping only the Fourier modes with wave numbers smaller than a UV cut-off $k_{\rm max}$.

Expressing ψ in terms of the Fourier modes $A_{\mathbf{k}}$ as

$$\psi(\mathbf{x},t) = \sum_k A_{\mathbf{k}}(t)e^{i\mathbf{k}\cdot\mathbf{x}}, \quad \text{with} \quad \frac{\mathbf{k}}{k_{\rm min}} \in \mathbb{Z}^3, \tag{16}$$

and where $k_{\rm min} = 2\pi/V^{1/3}$ is the smallest wave number. The Galerkin (Fourier) truncated Gross-Pitaevskii equation (TGPE) is defined as

$$-i\hbar\frac{\partial A_{\mathbf{k}}}{\partial t} = -\frac{\hbar^2k^2}{2m}A_{\mathbf{k}} - \sum_{\mathbf{k_1},\mathbf{k_2}} A_{\mathbf{k_1}}A^*_{\mathbf{k_2}+\mathbf{k_1}}A_{\mathbf{k}+\mathbf{k_2}}, \tag{17}$$

where the Fourier modes satisfy $A_{\mathbf{k}} = 0$ if $k \geqslant k_{\rm max}$ and the sum is performed over all wave numbers satisfying $|\mathbf{k_1}|, |\mathbf{k_2}|, |\mathbf{k_2} + \mathbf{k_1}|, |\mathbf{k} + \mathbf{k_2}| < k_{\rm max}$. This time-reversible finite system of ordinary differential equations with a large number of degree of freedom $\mathcal{N} \sim (k_{\rm max}/k_{\rm min})^3$ also conserves the energy, number of particles, and momentum.

The direct numerical evaluation of the convolution in Eq. (17) would be very expensive in computational time $O(N^6)$, where N is the resolution. This difficulty is avoided by using pseudospectral methods [34] and the nonlinear term is calculated in physical space, using FFTs that reduce the CPU time to $O(N^3 \log N)$. Introducing the Galerkin projector $\mathcal{P}_G$ that reads in Fourier space $\mathcal{P}_G[A_{\mathbf{k}}] = \theta(k_{\rm max} - k)A_{\mathbf{k}}$ with $\theta(\cdot)$ the Heavside function, the TGPE (17) can be written as

$$i\hbar\frac{\partial\psi}{\partial t} = \mathcal{P}_G\left[-\frac{\hbar^2}{2m}\nabla^2\psi + g\mathcal{P}_G[|\psi|^2]\psi\right]. \tag{18}$$

Equation (18) exactly conserves energy and mass and, if it is correctly dealiased using the 2/3 rule [34] (dealiasing at $k_{\rm max} = \frac{2}{3}\frac{N}{2}$), it also conserves momentum (see Appendix A

for a explicit demonstration). The Galerkin truncation also preserves the Hamiltonian structure with the truncated Hamiltonian given by $H = \int d^3x(\frac{\hbar^2}{2m}|\nabla\psi|^2 + \frac{g}{2}[\mathcal{P}_G|\psi|^2]^2)$.

Let us remark that perhaps a more standard definition of dealiasing in Eq. (18) could have been $\mathcal{P}_G[|\psi|^2\psi]$ using 1/2 rule (dealiasing at $k_{\max} = \frac{1}{2}\frac{N}{2}$) rather than $\mathcal{P}_G[\mathcal{P}_G[|\psi|^2]\psi]$ with the 2/3 rule. Using the former definition removes the restriction $|\mathbf{k_2}| < k_{\max}$ on the convolution in Eq. (17). Both methods are equivalent in the partial differential equation (PDE) limit (exponential decay of energy spectrum for $k \ll k_{\max}$) and admit the same invariants. However, the scheme of Eq. (18) is preferable because $k_{\max}$ is larger at the same resolution. If dealiasing is not preformed in Eq. (18) the errors in the conservation of momentum can rise up to 50% in a few units of time (see Appendix A). In a finite difference scheme the conservation of momentum should also be checked carefully as it is bound to produce spurious effects.

Another effect caused by periodic boundary condition is that the velocity $\mathbf{v}_G$ in the Galilean transformation (12) is quantized by the relation

$$\mathbf{v}_G = \frac{\hbar}{m}\frac{2\pi}{V^{1/3}}\mathbf{n_G}, \tag{19}$$

where $\mathbf{n_G} \in \mathbb{Z}^3$ and $\mathbf{v}_G$ becomes continuous only in the limit $\hbar/(mV^{1/3}) \to 0$. The Galilean invariance is slightly broken by the TGPE (17) because of modes close to the truncation wave number $k_{\max}$. However, it is recovered in the PDE limit where high-wave-number modes are converging exponentially and also in the thermodynamic limit: $\frac{k_{\max}}{k_{\min}} \to \infty$ defined below because the offending terms represent only a surface effect in Fourier space.

3. Thermodynamical limit and statistical ensembles

Let us first note that the energy H, the number of particles N and the momentum $\mathbf{P}$ in Eqs. (2)–(4) are all proportional to the total number of modes $\mathcal{N} \sim k_{\max}^3 V$ and therefore are all extensive quantities. Also note that by definition of the coherence length (7), the number $\xi k_{\max}$ determines the amount of dispersion at truncation wave number in the system.

The thermodynamic limit $V \to \infty$ of the truncated Gross-Pitaevskii system is thus defined as the limit

$$\mathcal{N} \to \infty, \quad \xi k_{\max} = \text{const.}, \tag{20}$$

in order to obtain equivalent systems. In this limit the relevant thermodynamic variables are the intensive quantities H/V, N/V, and $\mathbf{P}/V$. In practice, to perform numerical computations we will fix the volume to $V = (2\pi)^3$ and we will vary $k_{\max}$ (see paragraphs before Sec. III).

Let us define, as usual, the microcanonical ensemble [35] by the probability dw of finding the system in states with given values of energy H_{in}, number of particles N_{in} (the subscript "in" stands for initial data), and momentum $\mathbf{P}_{\text{in}}$ given by:

$$dw = \text{const.}\, e^S \delta(H - H_{\text{in}})\delta(N - N_{\text{in}}) \times \delta^3(\mathbf{P} - \mathbf{P}_{\text{in}}) dH dN d^3P, \tag{21}$$

where $S = \log\Gamma$ is the entropy with Γ the number of accessible microstates.

Microcanonical statistical states can be obtained numerically by time integrating the TGPE until the system reaches thermodynamic equilibrium [13,27]. These thermalized states are formally determined by the control values H_{in}, N_{in}, and $\mathbf{P}_{\text{in}}$ that are set in the initial condition. It has been shown in Refs. [13,27] by varying the values of H_{in} that TGPE present a phase transition analogous to the one of Bose-Einstein condensation, where the amplitude at 0-wave-number $A_{\mathbf{0}}$ vanishes for finite values of H_{in}. Let us remark that an explicit expression of dw or S cannot be easily obtained in the microcanonical ensemble and therefore the temperature is not easily accessible.

A simple way to explicitly control the temperature is to use the canonical or grand-canonical formulation. The grand-canonical distribution probability is given by a Boltzman weight

$$\mathbb{P}_{\text{st}} = \frac{1}{\mathcal{Z}} e^{-\beta F} \tag{22}$$

$$F = H - \mu N - \mathbf{W}\cdot\mathbf{P}, \tag{23}$$

where $\mathcal{Z}$ is the grand partition function, β is the inverse temperature, and μ is the chemical potential. In what follows we will refer to $\mathbf{W}$ as the counterflow velocity. Note that when $\mathbf{W} = 0$, $F = H - \mu N$ and the statistic weight of distribution (22) corresponds to the so-called $\lambda\phi^4$ theory studied in second-order phase transitions [31,32]. This point will be further discussed in Sec. III C.

Finally remark that the states with $\mathbf{W} \neq 0$ are obtained, in the thermodynamic limit, by a Galilean transformation of the basic $\mathbf{W} = 0$ state [see below Eq. (72)]. However, for finite size systems, because of the quantification of the Galilean transformation [Eqs. (12) and (19)] new metastable states with counterflow appear. These metastable states and their interactions with vortices will be studied in detail below in Sec. V A.

In the grand-canonical ensemble [Eqs. (22) and (23)], the mean energy $\overline{H}$, number of particles $\overline{N}$, and momentum $\overline{\mathbf{P}}$ are easily obtained by defining the grand-canonical potential

$$\Omega = -\beta^{-1}\log\mathcal{Z} \tag{24}$$

and using the relations

$$\overline{N} = -\frac{\partial\Omega}{\partial\mu}, \quad \overline{\mathbf{P}} = -\frac{\partial\Omega}{\partial\mathbf{P}}, \quad \overline{H} = \frac{\partial\Omega}{\partial\beta} + \mu\overline{N} + \mathbf{W}\cdot\mathbf{P}. \tag{25}$$

Observe that the microcanonical states (21) are characterized by the values H_{in}, N_{in}, and $\mathbf{P}_{\text{in}}$. On the other hand, the grand-canonical states are controlled by the conjugate variables: β, μ, and $\mathbf{W}$. The different statistical ensembles are expected to be equivalent in the thermodynamics limit (20) and therefore

$$H_{\text{in}} = \overline{H}, \quad N_{\text{in}} = \overline{N}, \quad \mathbf{P}_{\text{in}} = \overline{\mathbf{P}}, \tag{26}$$

in this limit. The equivalence of ensembles will be numerically tested below in Sec. III A.

In the grand-canonical ensemble, the pressure p is usually defined from the grand-canonical potential (24) by the relation [35] $\Omega = -pV$. This definition presents two problems in the TGPE system. First, due to classical statistics Ω has a logarithmic divergence at $\beta = \infty$. Second, this definition does not coincide with the standard relation in fluid dynamics

involving the diagonal part of the momentum flux tensor Π_{ij} [see Eq. (5)]. Both these problems can be solved by considering the total number of modes as a new thermodynamics variable, as we will see in the next section.

B. Thermodynamics of the truncated system

When a Galerkin truncation is performed on a system a new variable $k_{\max}$ explicitly appears. One thus find that the thermodynamic potentials depend on the total number of modes. Denoting $\lambda_{\mathcal{N}}$ the conjugate variable to the total number of modes $\mathcal{N}$ the standard thermodynamic relation for the energy easily generalizes as

$$dE = -pdV + TdS + \mu dN + \lambda_{\mathcal{N}} d\mathcal{N} + \mathbf{W}\cdot d\mathbf{P} \quad (27)$$

with S the entropy and where we have included the total momentum dependence $d\mathbf{P}$. As in Landau two-fluid model [1] Eq. (27) is written in a system of reference, where $\mathbf{v}_s = \overline{\nabla\phi} = \mathbf{0}$ (the bar standing for some ensemble average) and $E = \overline{H}$ is the macroscopic energy.[1] We will omit the bar over the others microscopic quantities. Note that the Fourier modes formally play the role of "particles" and $\lambda_{\mathcal{N}}$ is formally the "chemical potential" associated to those "particles."

The thermodynamic potentials can be easily generalized to take in to account the new variables. It is useful to define the Gibbs potential G, grand canonical Ω, and a generalized grand-canonical potential Ω' (with a Legendre transformation on $\mathcal{N}$) as

$$G = E - TS + pV - \mathbf{W}\cdot\mathbf{P} \quad (28)$$

$$\Omega = E - TS - \mu N - \mathbf{W}\cdot\mathbf{P} \quad (29)$$

$$\Omega' = E - TS - \mu N - \lambda_{\mathcal{N}}\mathcal{N} - \mathbf{W}\cdot\mathbf{P} \quad (30)$$

from where their respective variations follows:

$$dG = Vdp - SdT + \mu dN + \lambda_{\mathcal{N}} d\mathcal{N} - \mathbf{P}\cdot\mathbf{dW} \quad (31)$$

$$d\Omega = -pdV - SdT - Nd\mu + \lambda_{\mathcal{N}} d\mathcal{N} - \mathbf{P}\cdot\mathbf{dW} \quad (32)$$

$$d\Omega' = -pdV - SdT - Nd\mu - \mathcal{N}d\lambda_{\mathcal{N}} - \mathbf{P}\cdot\mathbf{dW}. \quad (33)$$

Based on standard arguments of extensive variables [35] and noting that $\lambda_{\mathcal{N}}$ and $\mathbf{W}$ are intensive variables we find the standard formula of the Gibbs potential with two types of particles

$$G = \mu N + \lambda_{\mathcal{N}}\mathcal{N}. \quad (34)$$

Using Eqs. (28) and (34) in Eqs. (29) and (30) we find

$$\Omega = -pV + \lambda_{\mathcal{N}}\mathcal{N}, \quad \Omega' = -pV. \quad (35)$$

The relations (27)–(35) determine all the thermodynamic variables and potentials. For instance, the pressure p can be obtained from Eqs. (32), (33), or (35) by

$$p = -\left.\frac{\partial\Omega}{\partial V}\right|_{T,\mu,\mathcal{N},\mathbf{W}} = -\frac{\Omega - \lambda_{\mathcal{N}}\mathcal{N}}{V} = -\frac{\Omega'}{V}, \quad (36)$$

where $\lambda_{\mathcal{N}} = \left.\frac{\partial\Omega}{\partial\mathcal{N}}\right|_{V,T,\mu,\mathbf{W}}$.

[1]The Galilean invariant expression of $\mathbf{W}$ is $\mathbf{V}_n - \mathbf{V}_s$ (see Sec. V).

We proceed now to show that thermodynamic definition (36) of the pressure coincides with the standard relation in fluid dynamics. In order to make explicit the dependence of the energy H on the volume V let us define the dimensionless space variables $\tilde{x} = x/V^{\frac{1}{3}}$ and $\tilde{\psi} = V^{1/2}\psi$. Expressed in term of these variables the Hamiltonian (2) reads $H = \int d^3\tilde{x}(\frac{\hbar^2}{2m}\frac{1}{V^{\frac{2}{3}}}|\tilde{\nabla}\tilde{\psi}|^2 + \frac{1}{V}\frac{g}{2}|\tilde{\psi}|^4)$. Taking the derivative with respect to V and reintroducing x and ψ yields

$$\frac{\partial H}{\partial V} = -\frac{1}{V}\int d^3x\left(\frac{\hbar^2}{2m}\frac{2}{3}|\nabla\psi|^2 + \frac{g}{2}|\psi|^4\right). \quad (37)$$

This expression corresponds to the spatial average of the diagonal part of Π_{ik} [see Eq. (5)]. As by definition $E = \overline{H}$ and the derivative has been implicitly done at constant total number of modes and momentum we find, using the thermodynamic relation (27) and Eq. (37), that the pressure satisfies

$$p = -\left.\frac{\partial E}{\partial V}\right|_{S,N,\mathcal{N},\mathbf{P}} = -\left.\overline{\frac{\partial H}{\partial V}}\right|_{N,\mathcal{N},\mathbf{P}}, \quad (38)$$

where the second equality holds for adiabatic compressions [35].

Finally, by replacing Ω in Eq. (29) we obtain the thermodynamic relation

$$E + pV - \mu N - \mathbf{W}\cdot\mathbf{P} = TS + \lambda_{\mathcal{N}}\mathcal{N}. \quad (39)$$

Let us remark that, in a classical system, the entropy is defined up to an additive constant related to the normalization of the phase space. However, the quantity $TS + \lambda_{\mathcal{N}}\mathcal{N}$ is completely determined because each term in the left-hand side of Eq. (39) is well defined. By the same arguments $d(\mathcal{N}\lambda_{\mathcal{N}}/T)$ is also a completely determined quantity. If the variable $\mathcal{N}$ had not been taken into account, the corresponding pressure would be $-\Omega/V$ and therefore wrongly defined and depending on the normalization constant. The grand-canonical potential Ω will be explicitly obtained at low temperature in Sec. III B where the above considerations can be explicitly checked.

C. Generation of grand-canonical distribution using a stochastic Ginzburg-Landau equation

Grand-canonical equilibrium states are given by the statistics [Eqs. (22) and (23)]. They cannot be easily obtained because the Hamiltonian H in Eq. (2) is not quadratic and therefore the statistical distribution is not Gaussian. Nevertheless, it is possible to construct a stochastic process that converges to a stationary solution with equilibrium distribution [Eqs. (22) and (23)]. This process is defined by a Langevin equation consisting of a stochastic Ginbzurg-Landau equation (SGLE) that reads

$$\hbar\frac{\partial A_{\mathbf{k}}}{\partial t} = -\frac{1}{V}\frac{\partial F}{\partial A^*_{\mathbf{k}}} + \sqrt{\frac{2\hbar}{V\beta}}\,\hat{\zeta}(\mathbf{k},t) \quad (40)$$

$$\langle\zeta(\mathbf{x},t)\zeta^*(\mathbf{x}',t')\rangle = \delta(t-t')\delta(\mathbf{x}-\mathbf{x}'), \quad (41)$$

where F is defined in Eq. (23) and $\hat{\zeta}(\mathbf{k},t)$ is the ($k_{\max}$-truncated) Fourier transform of the gaussian white-noise $\zeta(\mathbf{x},t)$ defined by

Eq. (41). The Langevin equation [Eqs. (40) and (41)] explicitly reads in physical space

$$\hbar\frac{\partial\psi}{\partial t} = \mathcal{P}_G\left[\frac{\hbar^2}{2m}\nabla^2\psi + \mu\psi - g\mathcal{P}_G[|\psi|^2]\psi - i\hbar W\cdot\nabla\psi\right] + \sqrt{\frac{2\hbar}{V\beta}}\mathcal{P}_G[\zeta(\mathbf{x},t)]. \quad (42)$$

In the $\beta\to\infty$ limit Eq. (42) reduces to the advective real Ginzurg-Landau equation (up to a redefinition of μ) that was introduced in Ref. [6]. This equation has the same stationary solutions of than the TGPE (18) in a system of reference moving with velocity $\mathbf{W}$. When the term $\mu\psi$ is also included in the TGPE it has, because of particle number conservation, the only effect of adding a global time-dependent phase factor to the solution.

The probability distribution $\mathbb{P}[\{A_{\mathbf{k}},A^*_{\mathbf{k}}\}_{\mathbf{k}<\mathbf{k}_{\max}}]$ of the stochastic process defined by Eqs. (40) and (41) can be shown to obey the following Fokker-Planck equation [36,37]

$$\frac{\partial\mathbb{P}}{\partial t} = \sum_{\mathbf{k}<\mathbf{k}_{\max}}\frac{\partial}{\partial A_{\mathbf{k}}}\left[\frac{1}{V\hbar}\frac{\partial F}{\partial A^*_{\mathbf{k}}}\mathbb{P} + \frac{1}{V\hbar\beta}\frac{\partial\mathbb{P}}{\partial A^*_{\mathbf{k}}}\right] + \text{c.c.} \quad (43)$$

It is straightforward to demonstrate that the probability distribution (22) is a stationary solution of Eq. (43), provided that βF is a positive defined function of $\{A_{\mathbf{k}},A^*_{\mathbf{k}}\}_{\mathbf{k}<\mathbf{k}_{\max}}$.

If one wishes to directly control, instead of the chemical potential μ, the value of the number of particles N or the pressure p, the SGLE must we supplied with one of two *ad hoc* equation for the chemical potential. These equation simply read

$$\frac{d\mu}{dt} = -\nu_N(N-N^*)/V \quad (44)$$

$$\frac{d\mu}{dt} = -\nu_p(p-p^*), \quad (45)$$

where the pressure p is computed as $p=-\frac{\partial H}{\partial V}$ [see Eq. (37)]. Equation (44) controls the number of particles and fixes its mean value to the control value N^*. Similarly Eq. (45) controls the pressure and fixes its value at p^*. Equations (44) and (45) are not compatible and they must not be used simultaneously. Depending on the type of temperature scans, the SGLE must be used together with either Eqs. (44) and (45) or alone with a fixed value of μ.

In the rest of this paper we will perform several numerical simulations of the TGPE (17) and SGLE (42). For numerics, the parameters in SGLE (omitting the Galerkin projector $\mathcal{P}_G$) will be rewritten as

$$\frac{\partial\psi}{\partial t} = \alpha_0\nabla^2\psi + \Omega_0\psi - \beta_0|\psi|^2\psi - i\mathbf{W}\cdot\nabla\psi + \sqrt{\frac{k_BT}{\alpha_0}}\zeta,$$

with similar changes for TGPE.

In terms of α_0, Ω_0, and β_0 the physical relevant parameters are the coherence length ξ and the velocity of sound c defined in Sec. II A 1 [see Eq. (7) and the text before]. They can be are expressed as

$$g\xi = \sqrt{\alpha_0/\Omega_0}, \qquad c=\sqrt{2\alpha_0\beta_0\rho^*} \quad (46)$$

with $\rho^*=\Omega_0/\beta_0$. The value of the density at $T=0$ set to $\rho^*=1$ in all the simulations presented below. In order to keep the value of intensive variables constant in the thermodynamic limit (20), with V constant and $k_{\max}\to\infty$ the inverse temperature is expressed as $\beta=1/k_{\mathcal{N}}T$, where $k_{\mathcal{N}}=V/\mathcal{N}$. With these definitions the temperature T has units of energy per volume and $4\pi\alpha_0$ is the quantum of circulation.

With ξ fixed, the value of ξ/c determines only a time scale. The velocity of sound is (arbitrarily) set to $c=2$ and the different runs presented below are obtained by varying only the coherence length ξ, the temperature T, the counterflow velocity $\mathbf{W}$, and the UV cutoff wave number $k_{\max}$. The number $\xi k_{\max}$ is kept constant (at the value $\xi k_{\max}=1.48$) when the resolution is changed, except in Sec. IV B where dispersive effects are studied (using a larger $\xi k_{\max}$). This choice of ξ ensures that vortices are well resolved [e.g., compare Fig. 5(a) below with Fig. 12 of Ref. [6]]. In the present work we use resolutions varying from 32^3 to 512^3 colocation points ($k_{\max}=10$ to 170, respectively). Finally in all numerical results the energy and momentum are presented per unit of volume $V=(2\pi)^3$ and the control values of number of particles and pressure in Eqs. (44) and (45) are set to $mN^*/V=\rho^*=1$ and $p^*=c^2\rho^{*2}/2=2$. Numerical integrations are performed with periodic pseudospectral codes and the time-stepping schemes are Runge-Kutta of order 4 for TGPE and implicit Euler for SGLE.

III. CHARACTERIZATION OF THERMODYNAMIC EQUILIBRIUM

In this section, the thermodynamic equilibrium is explored and characterized. The microcanonical and grand-canonical distributions are first shown to be numerically equivalent in a range of temperatures by comparing the statistics of GPE- and SGLE-generated states in Sec. III A. The steepest descent method is then applied to the grand-partition function in Sec. III B to obtain exact analytical expressions for the low-temperature thermodynamic functions. The basic numerical tools are validated by reproducing these low-temperature results. In Sec. III C a standard finite-temperature second-order λ phase transition is exhibited using the SGLE-generated grand-canonical states and the deviations to low-temperature equipartition are characterized.

A. Comparison of microcanonical and grand-canonical states

We now numerically compare the statistics of the grand-canonical states produced by the new algorithm SGLE to the statistics of the microcanonical states obtained by long-time integrations of TGPE. The coherence length is set to $\xi=\sqrt{2}/10$ and 32^3 collocation points are used ($k_{\max}=10$). The initial condition for the TGPE runs are chosen with random phases in a similar way than in Refs. [13,27]. We obtain low, medium, and high values of the energy with constant density $\rho=mN/V=1$ (see Table I).

To compare with the SGLE-generated statistics a scan in temperature at constant density $\rho=1$ is performed in order to obtain the temperature corresponding to the energies of the TGPE runs. Using the thermalized final states obtained from TGPE and converged final states of SGLE histograms of the of the density $\rho(x)$ in physical space are confronted in Fig. 1. They are found to be in excellent agreement.

TABLE I. Parameters of TGPE initial condition and time steps.

H	T	TGPE time steps	SGLE time steps
0.09	0.09	40 000	9600
0.5	0.5	20 000	9600
1.96	1.8	20 000	9600
4.68	4	20 000	5000

Observe that when the energy (or temperature) increases more weight becomes apparent on the histograms near $\rho = 0$, indicating the presence of vortices. The Gaussian character of the histogram in Fig. 1 a motivates the low-temperature calculation of the next section. Observe that, even at this relatively low 32^3 resolution, the thermodynamic limit has been reached in the sense that the micro and grand-canonical distribution coincide. We can thus safely use, at 32^3 and higher resolutions, the SGLE to prepare absolute equilibria of the TGPE.

Let us finally remark that the SGLE numerically converges much more rapidly toward absolute equilibrium than the TGPE, as displayed in Table I. Also taking into account the (computationally expansive) accurate conservative temporal scheme needed for the integration of the TGPE, the SGLE yields a (very) large economy of the CPU time needed to reach equilibrium. On the local machines where these computations were performed the SGLE was typically more than 10 times faster than TGPE.

B. Low-temperature calculation

The Gaussian histogram of Fig. 1(a) strongly suggests that some quadratic approximation should be able to obtain exact analytical expressions for the thermodynamic functions at low temperatures. In this section we use a such an approximation to compute the grand partition function $\mathcal{Z}$ and the grand-canonical potential[2] $\Omega = -\beta^{-1} \log \mathcal{Z}$ defined in Eq. (29).

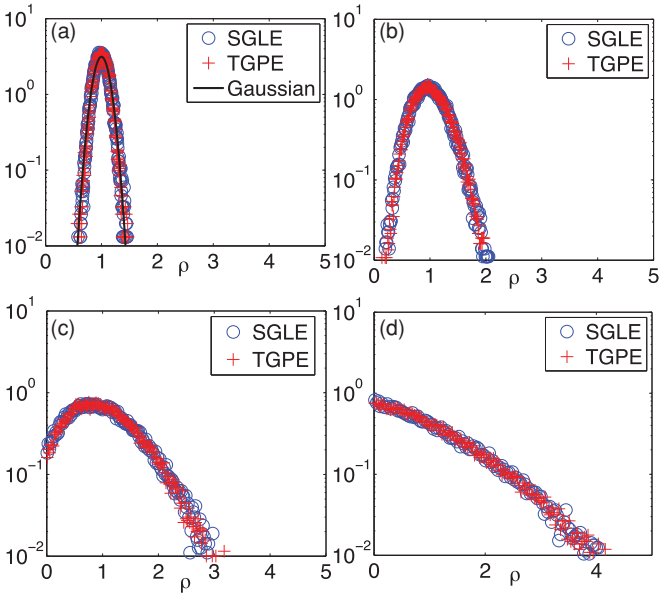

FIG. 1. (Color online) Comparison of density histograms obtained by SGLE and TGPE dynamics ($\xi = 2/10\sqrt{2}$ and resolution 32^3) with energy equal to (a) $H = 0.09$, (b) $H = 0.51$, (c) $H = 1.96$, and (d) $H = 4.68$ (see Table I). The solid line in (a) is a Gaussian of standard deviation $\delta\bar{\rho}^2 = 0.016$ [see below Eq. (60)] computed with the low-temperature calculations of Sec. III B.

The first step is to express the energy F of Eq. (23) in terms of the Fourier amplitudes $A_{\mathbf{k}}$. This leads to a nonquadratic function $F[A_{\mathbf{k}}, A^*_{\mathbf{k}}]$ explicitly given in Appendix B [Eqs. (B1)–(B3)]. The grand partition function is a product integral over all the Fourier amplitudes

$$\mathcal{Z}(\beta,\mu,\mathbf{W}) = V^{\mathcal{N}} \int \frac{dA_{\mathbf{0}} dA^*_{\mathbf{0}}}{2\pi} \prod_{\mathbf{k}<\mathbf{k}_{\max}} \frac{dA_{\mathbf{k}} dA^*{}_{\mathbf{k}}}{2\pi} e^{-\beta F[A_{\mathbf{k}}, A^*_{\mathbf{k}}]}. \tag{47}$$

The integrals in (47) cannot be done explicitly; however, it is possible to give a low-temperature approximation using the method of *steepest descent* [31,39]. We also add to F an *external field* with value $-\mu_0 |A_{\mathbf{0}}|^2 V$ in order to explicitly obtain the mean value of condensate Fourier mode $|A_{\mathbf{0}}|^2$ by direct differentiation. The physical partition function is finally obtained by setting $\mu_0 = 0$. The integrals are dominated by the saddle-point determined by $\frac{\partial F}{\partial A^*_{\mathbf{k}}} - \mu_0 A_{\mathbf{0}} V \delta_{\mathbf{k},\mathbf{0}} = 0$ that yields the solution [see Eqs. (B4) and (B5)]

$$g|A_{\mathbf{0}}|^2|_{\rm sp} = \mu + \mu_0 \quad A_{\mathbf{k}}|_{\rm sp} = 0 \quad \text{for } \mathbf{k} \neq \mathbf{0}, \tag{48}$$

where the subscript "sp" denotes saddle point. Note that in general $|A_{\mathbf{0}}|^2 \neq |A_{\mathbf{0}}|^2|_{\rm sp}$ and the mean value is equal to the saddle point one only at $T = 0$. Other solutions that can be obtained when $\mathbf{W} \neq 0$ will be discussed in detail in Sec. V.

At the saddle point (48) $A_{\mathbf{k}}$ vanishes for $\mathbf{k} \neq \mathbf{0}$. We thus need to keep only quadratic terms in $A_{\mathbf{k}}$ to obtain the low-temperature approximation. Using the notation $\mathbf{p} = \hbar\mathbf{k}$, at leading order F can be rewritten as $F = F_0 + F_1 + F_2$ with

$$F_0 = V\left(\frac{g}{2}|A_{\mathbf{0}}|^4 - \mu|A_{\mathbf{0}}|^2\right) \tag{49}$$

$$F_1 = V \sum_{\mathbf{p}\neq\mathbf{0}} \left(\frac{p^2}{2m} - \mu + 2g|A_{\mathbf{0}}|^2 - \mathbf{W}\cdot\mathbf{p}\right)|A_{\mathbf{p}}|^2 \tag{50}$$

$$F_2 = V\frac{g}{2} \sum_{\mathbf{p}\neq\mathbf{0}} A^{*2}_{\mathbf{0}} A_{\mathbf{p}} A_{-\mathbf{p}} + A^2_{\mathbf{0}} A^*_{\mathbf{p}} A^*_{-\mathbf{p}}. \tag{51}$$

In order to obtain the low-temperature partition function we need to compute the determinant of the matrix $\frac{\partial^2 F}{\partial A_{\mathbf{p}} \partial A_{\mathbf{q}}} - \mu_0 V \delta_{\mathbf{p},\mathbf{0}} \delta_{\mathbf{q},\mathbf{0}}$. This determinant can be obtained by making use of the Bogoliubov transformation

$$A_{\mathbf{p}} = u_p B_{\mathbf{p}} + v_p B^*_{-\mathbf{p}} \tag{52}$$

with $u_p = \frac{A_{\mathbf{0}}}{|A_{\mathbf{0}}|} \frac{1}{\sqrt{1-L_p^2}}$ and $v_p = \frac{A_{\mathbf{0}}}{|A_{\mathbf{0}}|} \frac{L_p}{\sqrt{1-L_p^2}}$ and where L_p is determined by imposing the diagonalization of $F - \mu_0 |A_{\mathbf{0}}|^2 V$. L_p is explicitly given in Eq. (B6). It is easy to show that (52) is a canonical transformation and that the normalization condition of the corresponding Poisson bracket implies $|u_p|^2 - |v_p|^2 = 1$.

[2]Grand-canonical computations avoid difficulties that are present in the canonical ensemble with the explicit conservation of the number of particles (see Sec. 2.2 of Ref. [38] and references therein).

Expressing F in the Bogoliubov basis we obtain

$$F = V\left[\frac{g}{2}|A_{\mathbf{0}}|^4 - \mu|A_{\mathbf{0}}|^2 + \sum_{\mathbf{p}\neq\mathbf{0}}(\epsilon(p;\mu,\mu_0) - \mathbf{W}\cdot\mathbf{p})|B_{\mathbf{p}}|^2\right] \tag{53}$$

with the dispersion relation (see Appendix B)

$$\epsilon(p;\mu,\mu_0) = \sqrt{\left(\mu + 2\mu_0 + \frac{p^2}{2m}\right)^2 - (\mu+\mu_0)^2}. \tag{54}$$

Let us recall that the exited modes $B_{\mathbf{p}}$ are called phonons in quantum mechanics. In the present classical case, because of classical statistics and quadratic Hamiltonian, there will be equipartition among phonon modes. Replacing the value of the chemical potential with its saddle-point expression $\mu = g|A_{\mathbf{0}}|^2\big|_{\rm sp}$ (at $\mu_0 = 0$), Eq. (54) yields the (standard; see Ref. [40]) Bogoliubov dispersion relation $\epsilon(p) = p\sqrt{\frac{g|A_{\mathbf{0}}|^2}{m} + \frac{p^2}{4m^2}}$. Note that $\epsilon(p)$ can also be directly obtained from the GPE by expressing ψ in hydrodynamics variables, using the Madelung transformation (6) and linearizing around an homogenous density $\rho_0 = m|A_{\mathbf{0}}|^2$ [6].

The partition function now trivially factorizes in independent parts $\mathcal{Z}(\beta,V,\mu,\mathbf{W},\mathcal{N},\mu_0) = \mathcal{Z}_0(\beta,\mu,\mu_0)\prod_{\mathbf{p}\neq\mathbf{0}}\mathcal{Z}_{\mathbf{p}}(\beta,\mu,\mathbf{W},\mu_0)$, where

$$\mathcal{Z}_0(\beta,V,\mu,\mu_0) = \sqrt{2}\pi^3\sqrt{\frac{V}{g\beta}}e^{\frac{V\beta(\mu+\mu_0)^2}{2g}}, \tag{55}$$

$$\mathcal{Z}_{\mathbf{p}}(\beta,\mu,\mathbf{W},\mu_0) = \frac{1}{\beta(\epsilon(p;\mu,\mu_0) - \mathbf{W}\cdot\mathbf{p})}. \tag{56}$$

The total number of modes $\mathcal{N} = \sum_k 1$ and the grand-canonical potential

$$\Omega(\beta,V,\mu,\mathbf{W},\mathcal{N}) = -\beta^{-1}\left[\log\mathcal{Z}_0 + \sum_{\mathbf{p}\neq\mathbf{0}}\log\mathcal{Z}_{\mathbf{p}}\right] \tag{57}$$

are sums over all wave numbers from which all thermodynamic quantities can be directly obtained by using the thermodynamic relation (32).

Replacing the sum by an integral the expression for the number of modes reads

$$\mathcal{N} = \int_0^{P_{\rm max}}\frac{p^2V}{2\pi^2\hbar^3}\,dp = \frac{P_{\rm max}^3V}{6\pi^2\hbar^3}. \tag{58}$$

Setting $\mathbf{W} = (0,0,w)$ the integral form of Eq. (57) reads

$$\begin{aligned}\Omega(\beta,V,\mu,w,\mathcal{N}) &= -\frac{V(\mu+\mu_0)^2}{2g} + \int_0^{P_{\rm max}}\int_{-1}^{1}\frac{p^2V}{2\pi^2\hbar^3}\log\left(\beta\sqrt{\left(\mu+2\mu_0+\frac{p^2}{2m}\right)^2 - (\mu+\mu_0)^2} - \beta pwz\right)\frac{dz\,dp}{2}\\ &= -\frac{V(\mu+2\mu_0)}{2g} - \frac{P_{\rm max}^3V}{6\pi^2\beta\hbar^3}\left\{\frac{2}{3} - \log\left[\beta\epsilon(P_{\rm max};\mu)\right] - f\left[\frac{4m\mu}{P_{\rm max}^2}\right]\left(1 - \frac{w^2m}{2\mu}\right) - \frac{\mu_0}{\mu}f_0\left[\frac{4m\mu}{P_{\rm max}^2}\right]\right\}.\end{aligned} \tag{59}$$

In order to obtain Eq. (59) the thermodynamic limit (20) of infinite volume[3] was taken and the conditions $w^2 \ll \mu/m$, $\mu_0/\mu \ll 1$ were used. The functions $f[z]$ and $f_0[z]$ are explicited in Eqs. (B10) and (B11). Note that the dependence of the grand-canonical potential Ω on the number of modes $\mathcal{N}$ is implicitly given by $P_{\rm max}$ and Eq. (58). The first term in Ω is due to the condensed mode at $\mathbf{p} = 0$.

The low-temperature approximation to all thermodynamic functions is directly obtained from Eq. (59) by first setting $\mu_0 = 0$ and then differentiating (59), using relation (32). It is straightforward to check that both definition of the pressure in Eq. (36) coincide. Furthermore the higher-order moments of the density can be easily computed by taking successive derivatives of the grand-canonical potential. For instance, it is straightforward to show that the variance of the density ρ [see solid line on histograms displayed on Fig. 1(a)] is given by

$$V^2\langle\delta\rho^2\rangle = -\beta^{-1}m^2\frac{\partial^2\Omega}{\partial\mu^2}. \tag{60}$$

It can also be checked on the explicit expression for the entropy S [see Eqs. (B9)] that, as expected for a classical system, the entropy depends by a logarithmic term on the phase-space normalization. However, the function $TS + \lambda_{\mathcal{N}}\mathcal{N}$ is independent of phase-space normalization [see the discussion below Eq. (39)].

Finally, low-temperature expressions for the energies [Eqs. (8)–(10)] and their corresponding spectra can be easily obtained using Madelung's transformation (6). At low temperatures the fluctuations are small and $e_{\rm kin}$ depends only on ϕ and $e_q + e_{\rm int}$ only on ρ. The total energy is thus decomposed in two noninteracting terms. Equipartition of energy between the total kinetic energy $e_{\rm kin}$ and quantum plus internal energy $e_q + e_{\rm int}$ is thus expected at low temperature.

The next subsections will be concerned with the vanishing counterflow case $w = 0$. The states with nonzero counterflow w will be studied in details in Sec. (V).

C. λ transition and vortices

To characterize the condensation transition, we present here four temperature scans performed using SGLE (42). Three of them are at resolution of 64^3 with, respectively, constant chemical potential, density, and pressure [using Eqs. (44) and (45)]. The fourth scan is performed at constant pressure but at a resolution of 128^3. The coherence length is fixed so $\xi k_{\rm max} = 1.48$ is kept constant.

[3]The thermodynamic limit is taken over the grand-canonical potential $\Omega = -\beta^{-1}\log\mathcal{Z}$ as $V(\lim_{V\to\infty}\frac{\Omega}{V})$.

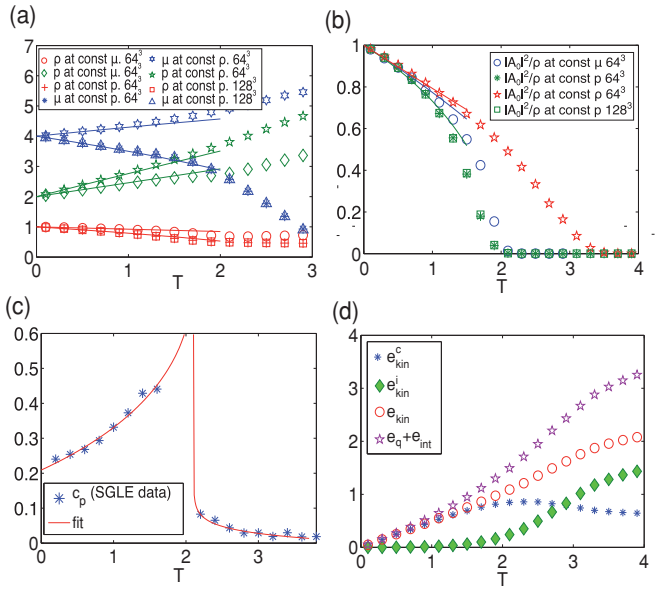

FIG. 2. (Color online) (a) Temperature dependence of the density ρ, pressure p, and chemical potential μ for SGLE scans at constant density, pressure, and chemical potential (see legend on figure). (b) Temperature dependence of the condensate fraction $|A_0|^2/\rho$ [same scans as in (a)]. (c) Specific heat $c_p = \frac{\partial H}{\partial T}|_p$ at constant pressure and resolution 128^3 the solid line corresponds to a fit [see Eq. (61)]. (d) Temperature dependence of the energies $e^c_{\rm kin}$, $e^i_{\rm kin}$, $e_{\rm kin}$ and $e_{\rm q} + e_{\rm int}$ at constant density; equipartition of energy between $e_{\rm kin}$ and $e_q + e_{\rm int}$ is apparent at low temperatures.

Figure 2(a) displays the results of the scans. Observe that the low-temperature behavior is in good agreement with the analytical calculations of Sec. III B and the explicit formulas given in Appendix B. Also observe that the constant pressure scans at resolutions of 64^3 and 128^2 coincide for all temperatures showing that the thermodynamic limit (20) discussed in Sec. II B is obtained at these resolutions.

Figure 2(b) displays the temperatures dependence of the condensate fraction $|A_0|/\rho$ for the four SGLE runs. Observe that the condensation transition previously obtained (in the constant density case) by microcanonical simulations in Refs. [13,27] is reproduced and also present (at different critical temperatures) in the constant pressure and chemical potential scans.

The SGLE algorithm directly provides the temperature as a control variable. It thus allows to easily obtain the specific heat from the data. Figure 2(c) displays the specific heat at constant pressure $c_p = \frac{\partial H}{\partial T}\big|_p$ for the scan at resolution 128^3. Let us note that the ($w = 0$) statistic weight of distribution [Eqs. (22) and (23)] corresponds to that of (standard two-component) second-order phase transitions [31,32]. We thus expect the condensation transition visible in Fig. 2(c) to be in this standard class. This point is confirmed by the solid lines in Fig. 2(c) that correspond to a fit with the theoretical prediction given by the renormalization group (RG)

$$c_p = \frac{A^\pm}{\alpha_{\rm RG}}|\tau|^{-\alpha_{\rm RG}}(1 + a_c^\pm|\tau|^\Delta + b_c^\pm|\tau|^{2\Delta} + \cdots) + B^\pm, \quad (61)$$

where $\tau = \frac{T-T_\lambda}{T_\lambda}$ and the $+$ and $-$ signs refer to $T > T_\lambda$ and $T < T_\lambda$; see Ref. [41]. The fit was obtained in the following way: First, the identification of the transition temperature T_λ was done by finding the zero of the linear interpolation of the second-order difference of H, discarding the three closest point to the zero of $|A_0|^2/\rho$. Then, using the critical exponents $\alpha_{\rm RG} = -0.011\,26$ and $\Delta = 0.529$ given by the RG, the data were fitted as in Ref. [41] over the nonuniversal constant. The obtained values are $A^+/A^- = 1.42$, to be compared with 1.05 in Ref. [41]. This discrepancy is probably due to finite size effects.

Finally, in Fig. 2(d) the temperature dependence at constant density of the different energies [Eqs. (8)–(10)] expressed in terms of hydrodynamical variables is displayed. Observe that the incompressible kinetic energy $E^i_{\rm kin}$ vanishes for low temperatures $T \ll T^\rho_\lambda$, where $T^\rho_\lambda = 3.31$ is the transition temperature at constant density. This vanishing is connected to the disappearance of vortices, and it is also manifest in the density histograms in Fig. 1. At low temperatures, equipartition of energy between the total kinetic energy $e_{\rm kin}$ and the quantum plus internal energy $e_q + e_{\rm int}$ (see the discussion at the end of Sec. III B) is apparent on Fig. 2(d).

IV. ENERGY CASCADE, PARTIAL THERMALIZATION, AND VORTEX ANNIHILATION

A new mechanism of thermalization through a direct cascade of energy is studied in Sec. IV A. Using initial conditions with mass and energy distributed at large scales, a long transient with partial thermalization of the density waves is obtained at small scales. Vortex annihilation is observed to take place and is related to mutual friction effects. A bottleneck effect that produces spontaneous self-truncation with partial thermalization and a time-evolving effective truncation wave number is characterized in Sec. IV B for large dispersive effects at the maximum wave number of the simulation.

A. Partial thermalization

We now study the (partial) thermalization of the superfluid Taylor-Green (TG) vortex. This flow, which was first introduced in Ref. [6], develops from an initial condition that is prepared by a minimization procedure using the advected real Ginzburg-Landau equation (ARGLE) [6]. The nodal lines of the initial condition $\psi_{\rm TG}$ are the vortex lines of the standard TG vortex and obeys all its symmetries. Numerical integrations are performed with a symmetric pseudospectral code, making use of the TG symmetries to speed up the computations and optimize memory use, as described in Ref. [6]. We use the equivalent to 64^3, 128^3, 256^3, and 512^3 collocation points and the coherence length is set such that, in all cases, $\xi k_{\rm max} = 1.48$.

Vortices and density fluctuations corresponding to the 512^3 run are visualized on Fig. 3 using the VAPOR[4] software. The short time behavior, see Figs. 3(a)–(c), corresponds to the GPE superfluid turbulent regime previously studied in Ref. [5]. A new TGPE thermalization regime where vortices

[4]http://www.vapor.ucar.edu.

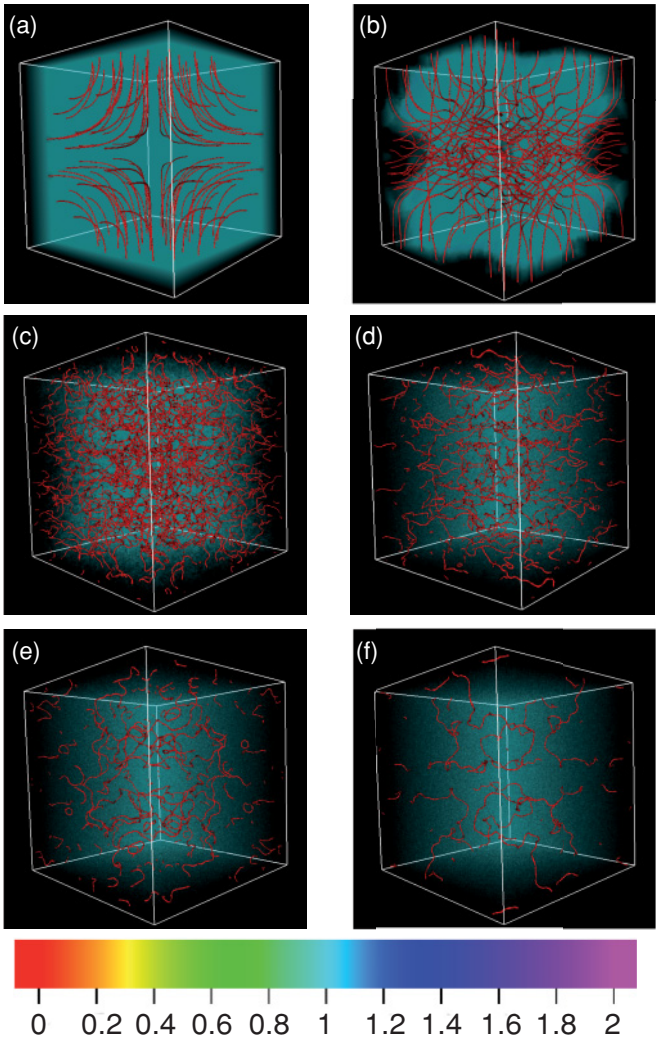

FIG. 3. (Color online) 3D visualization of density at $t = 0$, 5, 10, 20, 31, and 55 at resolution 512^3. Vortices are displayed as gray (red) isosurfaces and the gray (blue) clouds correspond to density fluctuations.

first reconnect into simpler structures and then decrease in size with the emergence of a thermal cloud is present at later times; see Figs. 3(d) and (e).

To further study this new TGPE regime, the temporal evolution of $e_{\rm kin}$, $e^i_{\rm kin}$, $e^c_{\rm kin}$, $e_q + e_{\rm int}$ is shown on Fig. 4(a) and the corresponding energy spectra are displayed on Fig. 5. Observe that, at $t = 0$, $e^i_{\rm kin}$ contains almost all the energy because of the highly vortical initial condition.

The early times ($t \leqslant 15$) behavior corresponds to the PDE regime of the GPE (1) that was previously reported in Refs. [5,6]. An energy transfer is observed from $e^i_{\rm kin}$ to the other energies ($e^c_{\rm kin}$ and $e_{\rm int} + e_q$) that are associated to the density waves.

Continuing the temporal integration the spectral convergence to the GP partial differential equation is lost. The dynamics becomes influenced by the truncation wave numbers $k_{\rm max}$ and thermalization starts to take place. Two new regimes are observed. The first one for $20 \lesssim t \lesssim 80$ corresponds to a partial thermalization at small scales: see Fig. 5(b)–(d).

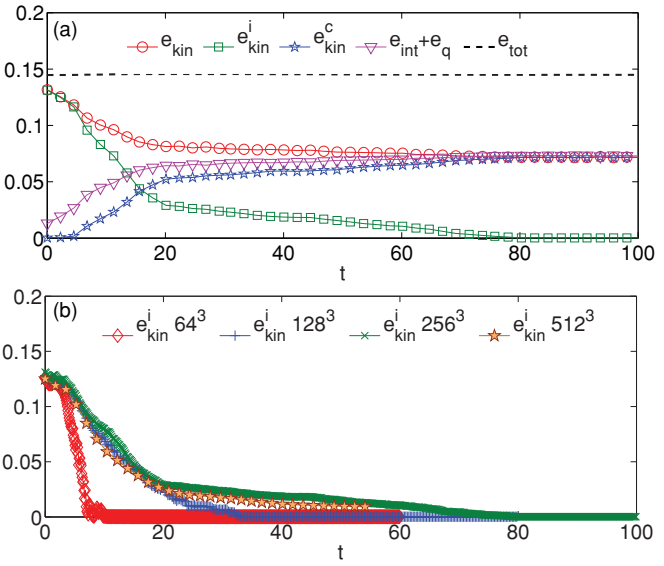

FIG. 4. (Color online) (a) Temporal evolution of energies $e^c_{\rm kin}$, $e^i_{\rm kin}$, $e_{\rm kin}$, and $e_q + e_{\rm int}$ at resolution 256^3. At large times, the incompressible energy vanishes and equipartition of energy between $e_{\rm kin}$ and $e_q + e_{\rm int}$ is observed. (b) Temporal evolution of $e^i_{\rm kin}$ at resolution of 64^3, 128^3, 256^3, and 512^3 with constant $\xi k_{\rm max} = 1.48$.

Observe that equipartition of $e^c_{\rm kin}$ and $e_q + e_{\rm int}$ begins to be established in this phase. The thermalized zone then progressively extends to larger wave numbers. During this phase $e^i_{\rm kin}$ decrease at almost constant rate [see Fig. 4(a)]. As shown on Fig. 4(b), this phase is delayed when the resolution is increased at constant $\xi k_{\rm max}$.

Around $t = 80$ [Figs. 4(a) and 5(d)] equipartition is established for each wave number and $e^i_{\rm kin}$ almost vanishes. This vanishing is related to the disappearance of vortex lines that first reconnect into simpler structures which then decrease in size and number and finally disappear (as can be directly observed on the density visualizations corresponding to the 256^3 run, pictures not shown). Note that the annihilation of the vortices can also be related to the contraction of vortex rings due to mutual friction reported in Ref. [30]. For $t > 80$ the system finally reaches the thermodynamic equilibrium. The final absence of vortices and equipartition of energy between $e^c_{\rm kin}$ and $e_q + e_{\rm int}$, as can be directly checked on the temperature scan in Fig. 2(d), is a consequence of the low energy of the initial condition $\psi_{\rm TG}$.

We have thus presented for the first time a new mechanism of thermalization through a direct cascade of energy of the TGPE similar to that of the incompressible truncated Euler equation reported in Ref. [21].

B. Dispersive slowdown of thermalization and bottleneck

We now turn to the study of dispersion effects on the thermalization of the TGPE dynamics and on vortex annihilation. To wit, we prepare three different initial conditions with different values of $\xi k_{\rm max}$ using the TG initial condition described in the preceding section. We fix the value of the coherence length to $\xi = \sqrt{2}/20$ and use resolutions of 64^3,

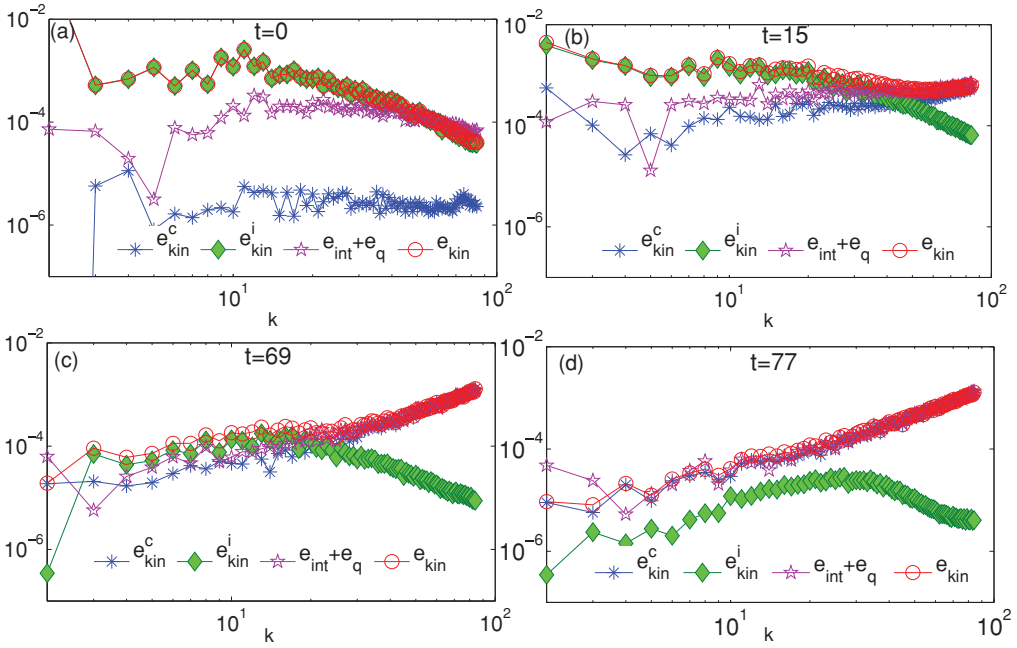

FIG. 5. (Color online) [(a)–(d)] Energy spectra at $t = 0$, 15, 69, 77 at resolution 256^3. (d) Equipartition is reached for all modes.

128^3, and 256^3 corresponding to $\xi k_{\max} = 1.48$, 2.97, and 6.01, respectively. The three initial condition therefore represent the same field at different resolutions. The temporal evolutions of $e_{\rm kin}$, $e^i_{\rm kin}$, $e^c_{\rm kin}$, and $e_q + e_{\rm int}$ for the three runs (indexed by the resolution) are displayed on Fig. 6(a).

They are identical until $t \approx 5$ where the run of resolution 64^3 starts to lose its spectral convergence. At at $t \approx 20$ all runs appear to have thermalized on Fig. 6(a). However, the kinetic energy spectra on Fig. 6(b) shows a clear difference between the runs (the dashed line corresponds to k^2 power-law scaling). The high-wave-number modes of the 64^3 run are thermalized. For the 128^3 run the high wave numbers begin to fall down and, at resolution 256^3, two zones are clearly distinguished. An intermediate thermalized range with an approximative k^2 power-law scaling is followed by a steep decay zone well before $k_{\max} = 85$. Remark that in the 256^3 run the spectral convergence is still ensured and the (partial) thermalization is thus obtained within the GP PDE dynamics.

The temporal evolution of $e_{\rm kin}(k)$ for the 256^3 run is displayed in Fig. 6(c). The large wave number k^{-3} power-law behavior at $t = 0$ is an artifact of the high-k decomposition of energies in the presence of vortices (see pp. 2649–2650 of Refs. [6] and [42]) and a faster decay is recovered as soon as the vortices disappear. The thermalized intermediate zone is observed to slowly extends to smaller wave numbers. This naturally defines a *self-truncation* wave number $k_c(t)$, where the energy spectrum starts to drastically decrease.

In order to determine $k_c(t)$ we have tested fits to $e_{\rm kin}(k)$ using two type of trial spectra with three free parameters: $e_{\rm fit\,I}(k) = A(t)k^{-n}\exp[-2\delta(t)k]$ and $e_{\rm fit\,II}(k) = A(t)k^{-n}\exp[-\gamma(t)k^2]$. The $e_{\rm fit\,II}(k)$ fit was found to work better in the sense that it both gives the correct $n = -2$ prefactor at intermediate and large times and also gives a better fit to the data at high k (data not shown). Fixing the prefactor at the value $n = -2$, we finally define our working two-parameter fit as

$$e_{\rm fit}(k,t) = A(t)k^2 e^{-[(\frac{9\pi}{16})^{\frac{1}{3}}(\frac{k}{k_c(t)})^2]} \tag{62}$$

$$e_{\rm fit}(t) = \int_0^{k_{\max}} e_{\rm fit}(k,t)\,dk. \tag{63}$$

The factor $(9\pi/16)^{1/3}$ in Eq. (62) was set in order to obtain the limits $Ak_c^3/3$ and $Ak_{\max}^3/3$ for $e_{\rm fit}(t)$ when $k_{\max} \to \infty$ and $k_c \to \infty$, respectively. The fits are also displayed in Fig. 6(c). They are in good agreement with the data after vortices have disappeared. The temporal evolution of $e_{\rm fit}(t)$ is displayed in Fig. 6(a). It does converge to the thermalized value of the energy. Finally, the temporal evolution of the self-truncation wave number $k_c(t)$, which seems to have a well-defined limit at infinite resolution, is displayed in Fig. 6(d) for the three runs.

An open question is whether k_c is bounded in time in the PDE regime where $k_c \ll k_{\max}$. In other words, is thermalization of the $\xi k_{\max} \gg 1$ truncated system simply delayed or completely inhibited when $\xi k_{\max}$ is large enough? Note that this problem is related to the classical Fermi-Pasta-Ulam-Tsingu problem [43].

To try to answer this question within the Taylor-Green framework would be computationally very expensive as long runs should be performed at arbitrarily high resolutions. A simple alternative idea to study this problem is to use initial data for the TGPE generated by the SGLE with a variable truncation wave number $k_c^{\rm in}$, set to a target value of k_c, smaller than the maximum truncation wave number $k_{\max}$ allowed by the resolution. This SLGE-generated initial data can then be used to run the TGPE at a given value of ξk_c with arbitrarily large values of $\xi k_{\max}$. A number of runs were performed at resolution 64^3 with various values of $k_c^{\rm in}$, ξ, and initial energy $e^{\rm in}$ (see legend on Fig. 7). The result of these computations are compared with the above Taylor-Green runs (see Fig. 6)

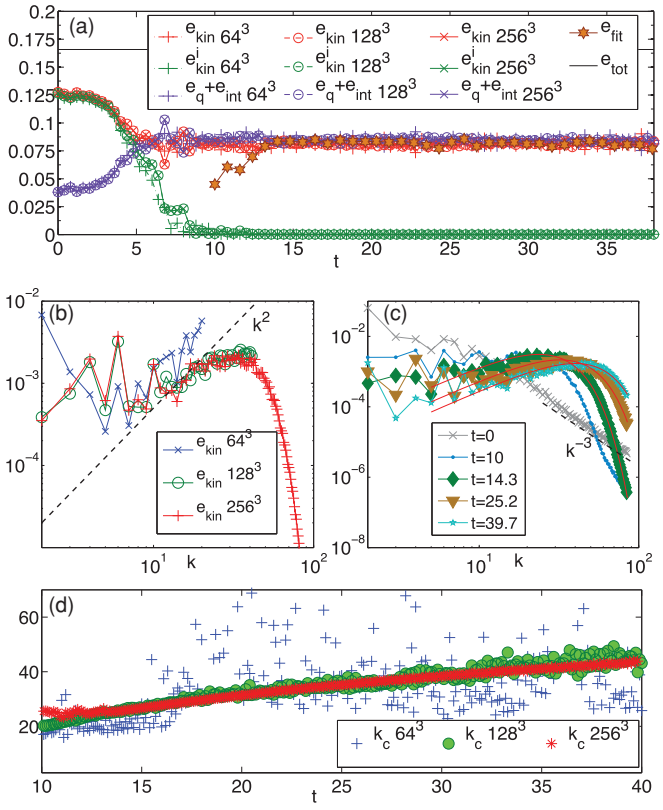

FIG. 6. (Color online) (a) Temporal evolution of energies [as in Fig. 4(a)] for $\xi k_{\max} = 1.48$, 2.97, and 6.01 (resolution 64^2, 128^3, and 256^3 respectively). Yellow stars are the kinetic energy reconstructed from fit data using Eq. (63). (b) Kinetic energy spectrum at $t = 17.4$ for $\xi k_{\max} = 1.48$, 2.97, and 6.01; the dashed black line indicates k^2 power-law scaling. (c) Temporal evolution of kinetic energy spectrum; the solid red lines correspond to fits using Eq. (62) and the dashes black line indicate k^{-3} power-law scaling. (d) Temporal evolution of effective self-truncation wave number k_c [Eq. (62)] at different resolutions.

and displayed on Fig. 7. Because of the steep decay of the energy spectrum for $k \gg k_c$, the self-truncation wave number is determined using the integral formula

$$k_c = \sqrt{\frac{5}{3}\frac{\int_0^{k_{\max}} k^2 e_{\rm kin}(k)\,dk}{\int_0^{k_{\max}} e_{\rm kin}(k)\,dk}}. \tag{64}$$

A general growth in time of k_c is apparent on Fig. 7(a) for both the Taylor-Green runs and the SGLE-generated initial data, showing similar behavior. In order to check for self-similar regime a parametric log-log representation dk_c/dt vs. k_c has been used on Fig. 7(b) and 7(c). With this representation, a self-similar evolution $k_c(t) \sim t^\eta$ corresponds to a line of slope $\chi = (\eta - 1)/\eta$. Figure 7(b) shows transient self-similar evolutions that all terminate by a vertical asymptote, corresponding to logarithmic growth ($\eta = 0$). This self-truncation takes place for small values of $k_c/k_{\max}$ strongly suggesting that the self-truncation happens in a regime independent of cutoff. Finally, Fig. 7(c) suggests that, depending on initial conditions, self-truncation can take place at arbitrarily values of ξk_c.

As the dynamics of modes at wave numbers larger than k_c is weakly nonlinear, it should be amenable to a description in terms of wave turbulence theory; this could perhaps explain the slowdown of the thermalization in this zone. The new regime indicates that total thermalization is delayed when increasing the amount of dispersion (controlled by $\xi k_{\max}$) but is preceded by a partial thermalization (quasiequilibrium up to k_c) *within* a PDE.

We now turn to estimations of order of magnitude relevant to physical BEC. At low-temperature, the GPE is known [3] to give an accurate description of the (classical) dynamics of physical BEC at scales larger than the interatomic separation ℓ. At finite temperature the TGPE gives a good approximation of Bose-Einstein condensate (BEC) only for the phonon modes with high occupation number; see Refs. [3,13]. At very low temperature, thus, only a limited range of low-wave-number density waves are in equipartition.

This limited range has consequences on the low-temperature thermodynamics of BEC that can be obtained by the following considerations. The equipartition range is determined by the relation $k \leqslant k_{\rm eq}$ with $\hbar\omega_B(k_{\rm eq}) = k_B T$, where the Bogoluibov dispersion relation $\omega_{\rm B}(k)$ is given by

$$\omega_B(k) = k\sqrt{\frac{g|A_0|^2}{m} + \frac{\hbar^2}{4m^2}k^2}. \tag{65}$$

The coherence length ξ defined in Eq. (7) can be expressed in terms of the s-wave scattering length $\tilde{a}$ defined by $g = 4\pi\tilde{a}\hbar^2/m$ and the mean interatomic particle distance $\ell \equiv n^{-1/3} \approx |A_0|^{-2/3}$ as

$$\xi = (8\pi n\tilde{a})^{-1/2} = \ell\frac{1}{\sqrt{8\pi}}\left(\frac{\ell}{\tilde{a}}\right)^{1/2}. \tag{66}$$

For weakly interacting BEC the coherence length thus satisfies $\xi \gg \ell$. The equipartition wave number $k_{\rm eq}$ explicitly reads

$$k_{\rm eq} = \left[\frac{\sqrt{4k_B^2 m^2 T^2 \xi^4 + \hbar^4}}{\xi^2\hbar^2} - \frac{1}{\xi^2}\right]^{1/2}. \tag{67}$$

Using the Bose-Einstein condensation temperature of non-interacting particles (valid for $\tilde{a} \ll \ell$) [3]

$$T_\lambda = \frac{2\pi\hbar^2}{k_B m}\left[\frac{n}{\zeta\left(\frac{3}{2}\right)}\right]^{2/3}, \tag{68}$$

where $\zeta(3/2) = 2.6124\ldots$, the equipartition wave number $k_{\rm eq}$ can be expressed as

$$k_{\rm eq} = \frac{1}{\xi}\left[\sqrt{1 + \frac{16\pi^2}{\zeta\left(\frac{3}{2}\right)^{4/3}}\frac{\xi^4}{\ell^4}\frac{T^2}{T_\lambda^2}} - 1\right]^{1/2}. \tag{69}$$

Observe that $k_{\rm eq}$ varies from $k_{\rm eq} = 0$ at $T = 0$ to a wave number of order $k_{\rm eq} \sim \ell^{-1}$ at T_λ and it is equal to $k_\xi = 2\pi/\xi$ at T^* defined by

$$T^* = 4\pi\sqrt{2 + 4\pi^2}\,\zeta\left(\frac{3}{2}\right)^{2/3}\frac{\tilde{a}}{\ell}T_\lambda. \tag{70}$$

Thus the thermodynamic of physical BEC at low-temperature (e.g., specific heat scaling as T^3) can be recovered from the TGPE thermodynamics by setting $k_{\max} = k_{\rm eq}(T)$.

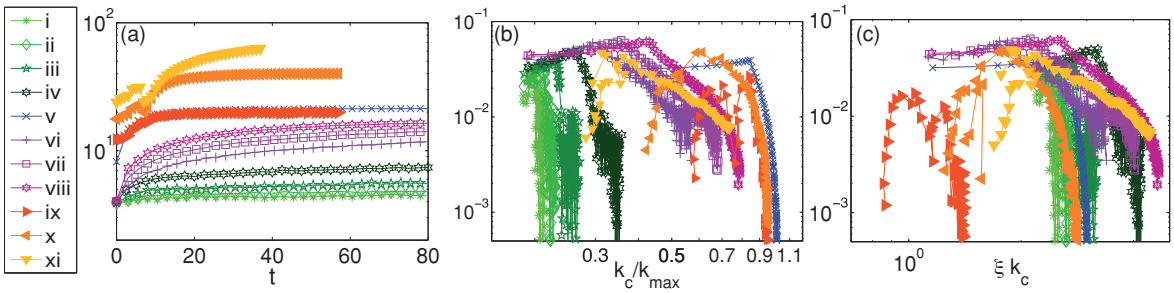

FIG. 7. (Color online) (a) Evolution of the self-truncation wave number k_c. Curves i–iv: $\xi = 2\sqrt{2}/5$, $k_c^{in} = 4$, $e^{in} = 0.1, 0.2, 0.4, 1$; v: $\xi = \sqrt{2}/10$, $k_c^{in} = 8$, $e^{in} = 0.2$; vi–viii: $\xi = \sqrt{2}/5$, $e^{in} = 0.1, 0.2, 0.4$ (i–viii in resolution 64^3); ix–xi: Taylor-Green resolutions 64^3, 128^3, and 256^3. [(b) and (c)] Parametric representation dk_c/dt vs. k_c/k_{max} and dk_c/dt vs. ξk_c [same labels as in (a)].

In experimental turbulent weakly interacting BEC such as in Ref. [44] the value of ξk_{eq} is large because $T^*/T_\lambda \sim \frac{a}{\ell} \ll 1$ and therefore the corresponding TGPE should have a large ξk_{max}. Thus the thermalization slowdown caused by the dispersive bottleneck should be in principle present in physical BEC, unless it is overwhelmed by other relaxation mechanisms [45].

V. METASTABILITY OF COUNTERFLOW, MUTUAL FRICTION, AND KELVIN WAVES

Counterflow states with nonzero values of momentum generated by the new SGLE algorithm and their interaction with vortices are investigated in this section. The counterflow states are shown to be metastable under SGLE evolution; the spontaneous nucleation of vortex ring and the corresponding Arrhenius law are characterized in Sec. V A. Dynamical counterflow effects are investigated in Sec. V B using vortex rings and vortex lines patterns that are exact solutions of the GPE. Longitudinal and transverse mutual friction effects are produced and measured. An anomalous translational velocity of vortex ring is exhibited and is quantitatively related to the effect of thermally excited finite-amplitude Kelvin waves. Orders of magnitude are estimated for the corresponding effects in BEC and superfluid ^{4}He.

A. Metastability of grand-canonical states with counterflow

1. Thermodynamic limit of states with nonzero counterflow

The counterflow states with $\mathbf{W} \neq \mathbf{0}$ are determined by thermal fluctuations around the minima of the energy F Eq. (23). These minima correspond to the solution of

$$\frac{\delta F}{\delta \psi^*} = 0 = -\frac{\hbar^2}{2m}\nabla^2\psi + g\mathcal{P}_G[|\psi|^2]\psi - \mu\psi + i\hbar\mathbf{W}\cdot\nabla\psi \tag{71}$$

that are plane waves of the form

$$\psi(x;\mathbf{v}_s) = g^{-\frac{1}{2}}\sqrt{\mu - m\mathbf{W}\cdot\mathbf{v}_s + \frac{mv_s^2}{2}}e^{-i\frac{m}{\hbar}\mathbf{v}_s\cdot\mathbf{x}}, \tag{72}$$

where the velocity $\mathbf{v}_s$ indexes the different solutions.

In the thermodynamic limit, the Galilean group defined by the transformations (12)–(15) is continuously indexed by the velocity $\mathbf{v}_G$. All wave functions (72) are thus equivalent by Galilean transformation (and redefinition of the chemical potential). Under the Galilean transformation (12) the energy F is transformed as $F' = F - (m\mathbf{W}\cdot\mathbf{v}_G - mv_G^2/2)N + \mathbf{v}_G\cdot\mathbf{P}$. Note that, among all the minima of F the one with $\mathbf{v}_s = \mathbf{W}$ minimizes F'. This state corresponds to a condensate moving with uniform velocity $\mathbf{W}$. The $\mathbf{W}\cdot\mathbf{P}$ term thus imposes only a Galilean transformation of the global minimum.

However, when working in a finite volume, the Galilean transformation is quantized [see Eq. (19)]. The minima of F' of lowest energy then corresponds to a condensate moving with the quantized uniform velocity $\mathbf{v}_s$ that is the closest to $\mathbf{W}$. At finite temperature and volume, when $\mathbf{W}$ is not too large with respect to the velocity quantum in Eq. (19), we have two ways to produce momentum in the system. The first one corresponds to Galilean transformations: $\mathbf{v}_s \neq 0$ in Eq. (72). The second one corresponds to fluctuations of the exited phonons, with $\mathbf{v}_s = 0$ in Eq. (72) and the momentum of phonons imposed by the term $\mathbf{W}\cdot\mathbf{P}$ in the grand-canonical distribution (22). Metastability is thus expected when $\mathbf{W} \neq 0$ with quasiequilibrium corresponding to condensates at different wave numbers with an energy barrier between each of those states.

In the context of the Landau two-fluid model [1] the velocity $\mathbf{v}_s$ of the condensate corresponds to the superfluid velocity and the momentum carried by the exited phonons is written as $\mathbf{P} = \rho_n(\mathbf{v}_n - \mathbf{v}_s)$ where ρ_n and $\mathbf{v}_n$ are called the normal density and velocity respectively. The counterflow velocity defined by $\widetilde{\mathbf{W}} = \mathbf{v}_n - \mathbf{v}_s$ is a Galilean invariant.

The above discussion shows that, in general the variable $\mathbf{W}$ in the SGLE (42) corresponds to $\mathbf{W} = \mathbf{v}_n$. In the thermodynamic (infinite volume) limit $\mathbf{W} = \mathbf{v}_s$ and there is thus no counterflow $\widetilde{\mathbf{W}} = \mathbf{v}_n - \mathbf{v}_s = \mathbf{0}$. For finite-size systems, in general $\mathbf{v}_s \neq \mathbf{W}$ and $\widetilde{\mathbf{W}} \neq \mathbf{0}$.

We thus define (when $v_s = 0$) the normal density by

$$\rho_n = \left.\frac{\partial P_z}{\partial w_z}\right|_{w_z=0}. \tag{73}$$

2. Thermodynamics of metastable states at small temperature and small counterflow

In order to first validate the SGLE in the presence of counterflow two scans are performed at constant density using a resolution of 64^3 and $\xi k_{max} = 1.48$. The condensate is set at $\mathbf{k} = 0$ in the SGLE initial data and the temperature is fixed to $T = 0.2$. This low temperature allows us to increase the value

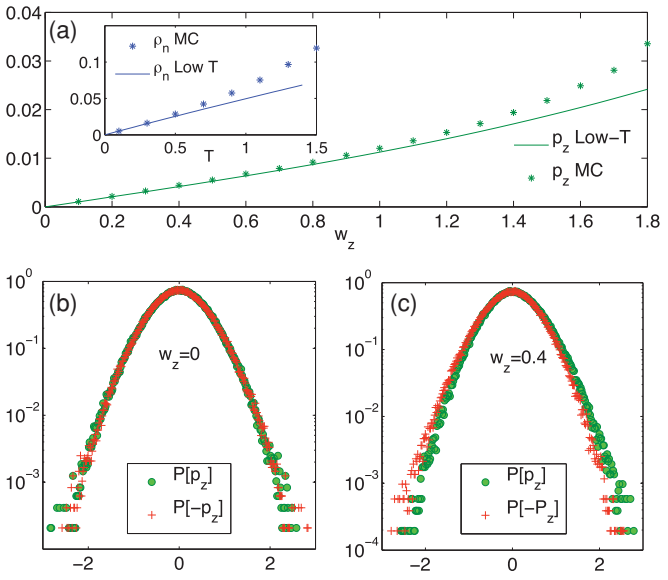

FIG. 8. (Color online) Counterflow dependence of momentum P_z ($w_x = w_y = 0$). (Inset) Temperature dependence of $\rho_n = \frac{\partial P_z}{\partial w_z}|_{w_z=0}$. (b) Histograms of momentum P_z and $-P_z$ (in log-lin) with no counterflow at $T = 1$. No asymmetry is observed. (c) Histograms of momentum P_z and $-P_z$ with counterflow $w_z = 0.4$ at $T = 1$. An asymmetry, induced by counterflow, is apparent. Observe that both histograms are centered at $P_z = 0$.

of the counterflow w_z (hereafter we set $w_x = w_y = 0$), keeping the condensate at $\mathbf{k} = 0$. The dependence of the momentum P_z on w_z is presented in Fig. 8(a). The solid line corresponds to the low-temperature calculations [Eq. (59) and Appendix B Eqs. (B9)]. The second run correspond to a temperature scan (at low counterflow $w_z = 0.1$). The temperature dependence of ρ_n is displayed together with the low-temperature calculation on the inset of Fig. 8(a).

Figures 8(a) and 8(b) display histograms of P_z and $-P_z$ in physical space, both obtained at $T = 1$ with the condensate at $\mathbf{k} = 0$ but with zero and nonzero counterflow. Observe that the histograms are both centered at $P_z = 0$ but the nonzero counterflow induces an asymmetry in the statistical distribution that yields a nonzero value for the mean momentum.

3. *Spontaneous nucleation of vortex rings and Arrhenius law*

At temperatures and counterflow velocities large enough the stochastic process defined by the SGLE can jump between the different metastable states discussed above in Sec. V A 1 . In this section, we show how the different states are explored, under SGLE evolution, by spontaneous nucleation of vortex rings. To wit, we present a numerical integration of SGLE at resolution 64^3 with $\xi k_{\max} = 1.48$. With this choice of parameters the velocity quantum (19) is fixed to 0.2. The temperature is set to $T = 0.775$ and the counterflow to $w_z = 0.8$. The condensate is set at $\mathbf{k} = \mathbf{0}$ in the SGLE initial data and the density is kept constant to $\rho = 1$.

The temporal evolution of the momentum P_z is displayed in Fig. 9(a) (right scale).

Observe that the system first spends some time at the state (I) with $P_z \approx 0.05$ and that, around $t = 55$, it jumps to the state (II) with $P_z \approx 0.225$. These two metastable states correspond

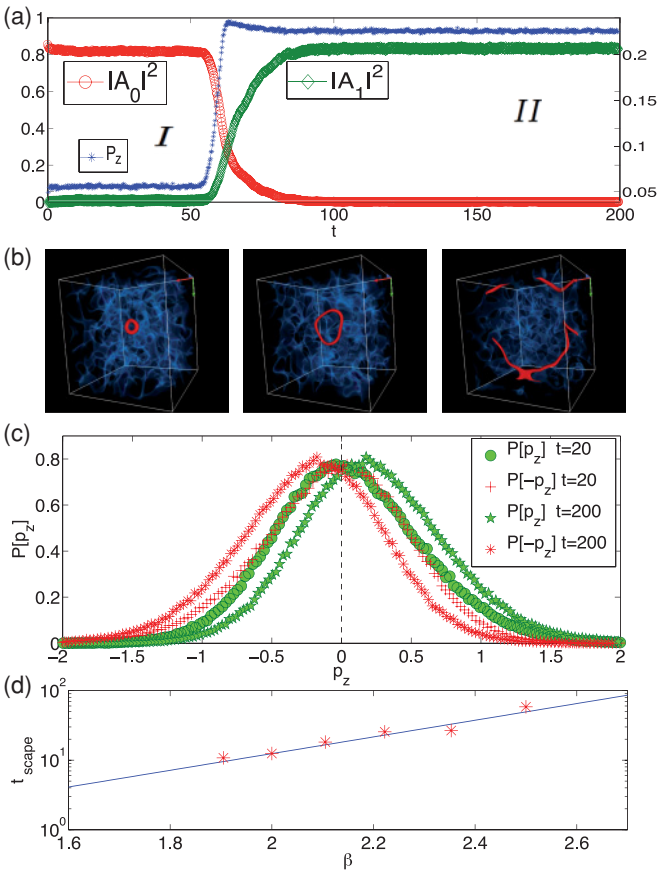

FIG. 9. (Color online) (a) Temporal evolution of $|A_0|^2$ and $|A_1|^2$ (left scale) under SGL dynamics. Observe that there are two quasistationary states (I and II) and the condensate makes a transition from $k = 0$ to $k = 1$. The temporal evolution of the momentum p_z is displayed in the same plot (right scale). Observe that transition from one state to the other is accompanied by an increase of momentum. (b) 3D visualization of density at $t = 54.5$, $t = 56$, and $t = 60.5$; the gray (blue) clouds corresponds to density fluctuations and the vortices are displayed as gray (red) isosurface (see the color bar in Fig. 12). (c) Histogram of momentum p_z and $-p_z$ at the two quasistationary states (I and II) in lin-lin plot. (d) Arrhenius law: data form SGL dynamics (points) and theoretical Eq. (74) (solid line).

to quasiequilibrium at $\mathbf{k} = \mathbf{0}$ and $\mathbf{k} = \mathbf{1}$ as is apparent in Fig. 9(a) (left scale) where the temporal evolution of $|A_\mathbf{0}|^2$ and $|A_\mathbf{1}|^2$ [see Eq. (16)] is displayed.

In order to illustrate the dynamic of the condensate jump from $\mathbf{k} = \mathbf{0}$ to $\mathbf{k} = \mathbf{1}$ we now present 3D visualization of the density at $t = 54.5$, $t = 56$, and $t = 60.5$ on Fig. 9(b). To produce this figure, the wave function ψ was first low-pass filtered and the density was then visualized using the VAPOR software. At early times ($t < 50$, pictures not shown) no vortices are present in the box. At $t \approx 54$ a vortex ring is nucleated. It then increases its size under SGLE evolution until it reconnects with the neighbor rings (recall that periodic boundary condition are used). The ring finally contracts and disappears (pictures not shown). During this evolution, the local phase defect of the ring becomes global and changes the condensate wave number. Histograms of momentum P_z and $-P_z$ in the two metastable states I and II are presented in Fig. 9(c). Observe that both momentum histograms of

metastable states are asymmetrical [as it was the case on Fig. 8(c)]. However, note that I is centered at $P_z = 0$ and II at $P_z = 0.2$, respectively, corresponding to the wave numbers $\mathbf{k} = \mathbf{0}$ and $\mathbf{k} = \mathbf{1}$.

It is well known that the escape time of a metastable quasiequilibirum is given, in general, by an Arrhenius law [46,47]

$$t_{\rm esc} \sim t_c e^{-\beta \Delta F}, \tag{74}$$

where ΔF is the activation energy of the nucleation solution and t_c is a characteristic time. Here, the nucleation solution is given by a vortex ring that satisfies $\frac{\partial F}{\partial \psi^*} = 0$. The energy barrier is thus determined by $\Delta F = H_{\rm ring}(R^*) - \mathbf{V}_{\rm ring} \cdot \mathbf{P}_{\rm ring}(R^*)$, where the analytic expressions for the energy $H_{\rm ring}$, the momentum $\mathbf{P}_{\rm ring}$, and the radius are given by

$$V_{\rm ring} = \frac{\hbar}{2m} \frac{1}{R^*} \left[\ln\left(\frac{8R^*}{\xi}\right) - a \right], \tag{75}$$

$$P^*_{\rm ring} = \frac{2\pi^2 \hbar \rho_\infty}{m} R^{*2}, \tag{76}$$

$$H^*_{\rm ring} = \frac{2\pi^2 \hbar^2}{m^2} \rho_\infty R^* \left[\ln\left(\frac{8R^*}{\xi}\right) - 1 - a \right], \tag{77}$$

where ρ_∞ is the density at the infinity and a is a core model-depending constant with value $a = 0.615$ for the GPE vortices [4]. Formulae (75)–(77) and the value of a have been numerically validated in Ref. [48] using a Newton method [49–51].

In order to numerically check that the escape time indeed follows an Arrhenius law we now perform runs with with $\xi k_{\rm max} = 1.48$ and resolution 32^3. The counterflow is fixed at $w = 1.4$ and the condensate is set initially at $\mathbf{k} = \mathbf{0}$ (constant density $\rho = 1$). At each fixed temperature T, several numerical integration of SGLE are performed and the escape times for the condensate to leave the wave number $\mathbf{k} = \mathbf{0}$ are measured. These escape times are then averaged over more than 10 realizations. Figure 9(d) displays the escape time $t_{\rm esc}$ obtained in this way as a function of the inverse temperature $1/T$ in log-lin. The slope of the solid line is computed using the analytic formulas (75)–(77) of ΔF. Both numerical and theoretical Arrhenius laws are in good agreement. The main consequence of this Arrhenius law is that it is practically possible to use the SGLE dynamics to prepare metastable states with finite value of counterflow and lifetime quantitatively given by (74).

B. Dynamical effects of finite temperature and counterflow on vortices

We now turn to the study the dynamical effects of counterflow on TGPE vortex evolution. To wit, we set up finite temperature and finite counterflow initial states that also contain vortices. Two cases are investigated: (i) vortex lines, in a crystal-like pattern that do not produce self-induced velocity, and (ii) vortex rings, producing self-induced velocity.

1. Lattice of vortex lines

To numerically study the effect of counterflow on vortices, we prepare an initial condition $\psi_{\rm lattice}$ consisting of a periodical array (of alternate sign) straight vortices. This initial condition is the 3D extension of that used in Ref. [52] to study the scattering of first sound in 2D. The lattice is obtained using a Newton method [49–51]. It is an exact stationary solution of the (periodic) GPE. As the vortices are separated by a fixed distance $d = \pi$, they can be considered isolated in the limit $\xi \ll d$. Let us remark that this limit is automatically obtained when the resolution is increased at constant $\xi k_{\rm max}$. To include temperature effect we prepare absolute equilibria $\psi_{\rm eq}$ using SGLE with the counterflow aligned with an axis perpendicular to the vortices in $\psi_{\rm lattice}$. The initial condition $\psi = \psi_{\rm lattice} \times \psi_{\rm eq}$ is then evolved using the TGPE. The counterflow induces a motion of the lattice as is apparent on the 3D visualizations of the the time evolution of the density that are displayed on Fig. 10 [figure obtained in the same way as Fig. 9(b)].

Several runs were performed at different resolutions (with $\xi k_{\rm max} = 1.48$), temperatures, and counterflow values [see legend on Fig. 11 (b)].

Figure 11(a) displays the temporal evolution of $(R_\parallel, R_\perp)$ the, respectively, parallel and perpendicular component of the vortex filament to the counterflow for $T = 0.5$, 1 and $w_z = 0.4$. The trajectories are obtained by first averaging along the direction of the vortices, then the (averaged) coordinate of the vortices is found by seeking the zero of the reduced $2d$ wave function. Observe that the vortex, originally located at $(\frac{3\pi}{2}, \frac{3\pi}{2})$, moves in the direction of the counterflow and its velocity clearly depends on the temperature. It is apparent that a perpendicular motion is also induced at short times. This motion has two phases, the first one is related to an

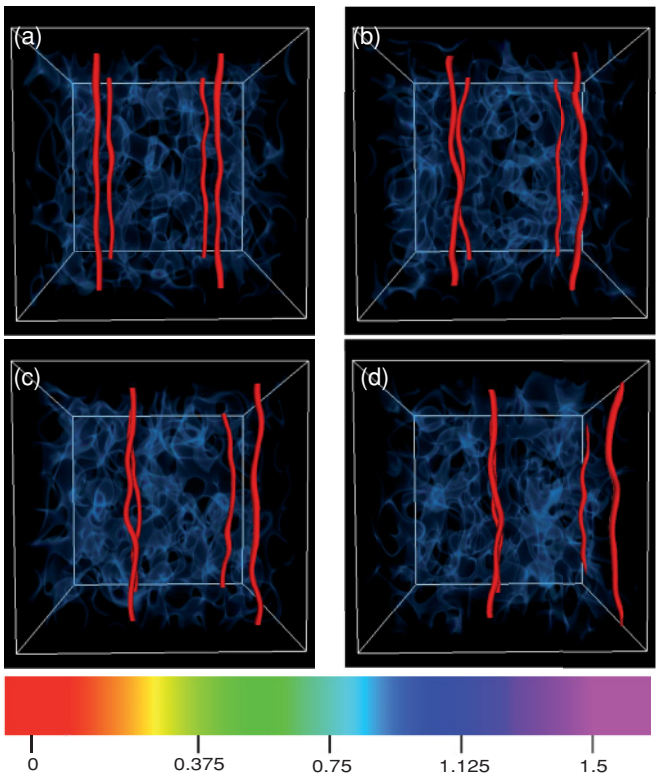

FIG. 10. (Color online) 3D visualization of density at $t = 0$, 40, 60, and 120 at temperature $T = 1$ and counterflow $W = 0.4$. The gray (blue) clouds correspond to density fluctuations and the crystal-like vortex lattice is displayed in gray (red) isosurfaces.

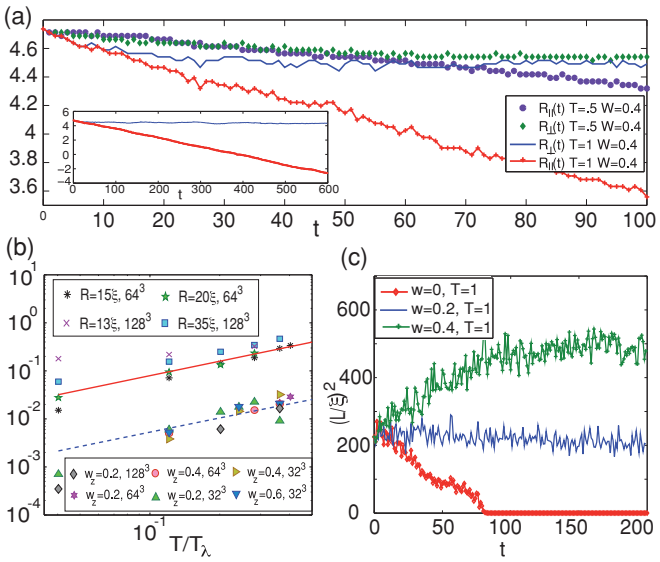

FIG. 11. (Color online) (a) Trajectory of a straight vortex in the crystal pattern for $T = 1$, $T = 0.5$, and $w_z = 0.4$ at resolution 64^3. (Inset) Run with $T = 1$ until $t = 600$. (b) Temperature dependence ($T_\lambda = 3.31$) of the advection velocity $v_\parallel/w_z$ for the lattice and $\Delta v_L/u_i$ for the vortex rings (resolutions 32^3–128^3). The dashed line corresponds to to Eq. (79) with $B' = 0.83$ and the solid line to the theoretical prediction (90). (c) Temporal evolution of the square of the length of the vortex ring for different values of counterflow, $T = 1$, and initial radius, $R = 15\xi$, at resolution 64^3.

adaptation and makes the crystal-like lattice slightly imperfect. The perpendicular motion then almost stops (a very small slope can be observed for long time integration). The initial phase where the parallel and perpendicular motions have similar velocities lasts longer when ξ/d is decreased by increasing the resolution (data not shown). Observe that the imperfection of the lattice in the final configurations is almost equal for the two temperatures presented in Fig. 11(a), but the parallel velocities differ considerably. Thus, the self-induced parallel velocity caused by the slight imperfection of the lattice is very small and is not driving the longitudinal motion.

We now concentrate on the measurement of $R_\parallel$ for which the present configuration is best suited. $R_\parallel$ has a linear behavior that allows direct measurement of the parallel velocity $v_\parallel$. The temperature dependence of $v_\parallel/w_z$ is presented on Fig. 11(b) for different values of w_z and d/ξ (corresponding to the different resolutions). For superfluid vortices the standard phenomenological dynamic equation of the vortex line velocity v_L is [4]

$$\mathbf{v}_L = \mathbf{v}_{\rm sl} + \alpha \mathbf{s}' \times (\mathbf{v}_n - \mathbf{v}_{\rm sl}) - \alpha' \mathbf{s}' \times [\mathbf{s}' \times (\mathbf{v}_n - \mathbf{v}_{\rm sl})], \quad (78)$$

where s' is the tangent to the vortex line, $\mathbf{v}_{\rm sl}$ is the local superfluid velocity (the sum of the ambient superfluid velocity v_s and the self-induced vortex velocity u_i), and $v_n = w + v_s$ is the normal velocity. The constants α,α' depend on the temperature. Let us note that the existence of the transverse force [related to the third term of right-hand side in Eq. (78)] has been subject of much debate in the low-temperature community in the latter part of the 1990s [53–59] and this controversy is still unresolved. Applied to the present case, Eq. (78) predicts $v_\perp = -\alpha w_z$ and $v_\parallel = \alpha' w_z$. The value of the constant α', related to the transverse force, depends on the normal density and the phonon-vortex scattering section. It can be expressed as

$$\alpha' = B' \frac{\rho_n}{2\rho}, \quad (79)$$

where B' is an order one constant [4]. A fit to the measured values of $v_\parallel/w_z$ yields $B' = 0.8334$; see Fig. 11(b). We thus conclude that finite-temperature TGPE counterflow effects measured on $R_\parallel$ for the crystal pattern are in quantitative agreement with standard phenomenology [Eq. (78)]. We have seen above that the effect on $R_\perp$ is of the same order of magnitude that the one on $R_\parallel$ but only in the initial phase as long as crystal imperfection does not come into play.

2. *Vortex rings*

We now turn to study the effect of counterflow on vortex rings. The initial condition is prepared as in the previous section but with the lattice $\psi_{\rm lattice}$ replaced by a vortex ring $\psi_{\rm ring}$, that is an exact stationary (in a comoving frame) solution of GPE. The plane containing the vortex rings of radius R is perpendicular to the counterflow and the rings are numerically obtained by a Newton method [49–51].

In the case of vortex rings the general formula (78) yields

$$\dot{R} = -\alpha(u_i - w_z), \quad (80)$$

$$v_L = v_s + (1 - \alpha')u_i + \alpha' w_z, \quad (81)$$

where u_i denotes the ring velocity at zero temperature, explicitly given by $V_{\rm ring}$ in formula (75) (replacing R^* by the corresponding radius). In the special simple case $w_z = 0$, a finite-temperature contraction of the vortex ring is predicted. This transverse effect effect was first obtained and measured by Berloff and Youd, using a finite-difference scheme version of the TGPE that exactly conserves the energy and particle number [30].

The temporal evolution of the square of the vortex length of a ring of initial radius $R = 15\xi$ at temperature $T = 1$ and counterflow $w_z = 0$, 0.2, and 0.4 is displayed on Fig. 11(c). For $w = 0$, the dynamics under TGPE evolution reproduces the Berloff ring contraction [30]. The temperature dependence of the contraction obtained for $w = 0$ (data not shown) quantitatively agrees with Berloff and Youd's results. A dilatation of vortex rings is apparent on Fig. 11(c) for w larger than the measured vortex ring velocity $v_L = 0.23$.

However, v_L has a very strong dependence on temperature that is also present for $w = 0$. The temperature dependence of $\Delta v_L/u_i$, where $\Delta v_L = u_i - v_L$, is displayed in Fig. 11(b). We have checked that the velocity v_L directly measured at $T = 0$ is indeed given by u_i. Equation (78) predicts (in the absence of counterflow) a translational velocity for the vortex ring $v_L = (1 - \alpha')u_i$. Observe that $\Delta v_L/u_i$ is one order of magnitude above the transverse mutual friction coefficient measured on the crystal-like lattice. Note the presence of a large spread of the low temperature data for the ring [see the leftmost data points in Fig. 11(b) corresponding to $T/T_\lambda = 0.04$]. At very low temperatures the effect is very weak. Thus, the corresponding measured values of $\Delta v_L/u_i$ are influenced by errors on the measurement of position and velocity of the vortices that are caused by the finite size of the mesh. In the future, these low temperature uncertainties on

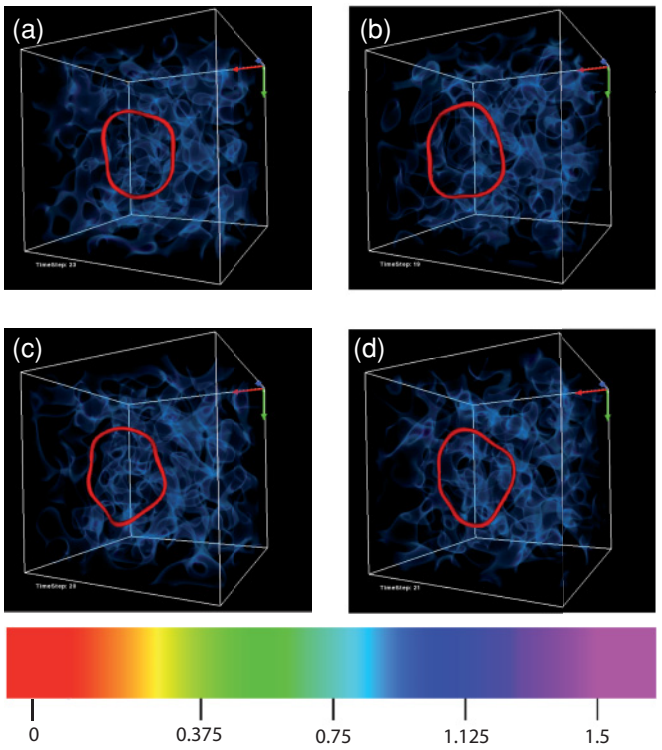

FIG. 12. (Color online) 3D visualization of density at $t = 18$, 19, 20, and 21 at temperature $T = 1$. The gray (blue) clouds correspond to density fluctuations and a vortex ring of radius $R = 20\xi$ with thermally excited Kelvin waves is displayed in gray (red) isosurfaces.

the determination of $\Delta v_L/u_i$ could be reduced by performing runs at higher resolution together with more accurate (subgrid) measurement of the vortex position.

3. *Anomalous translational velocity and Kelvin waves*

In this section we relate the finite temperature slowdown [see the top line of Fig. 11(b)] to the anomalous translational velocity of vortex ring with the finite-amplitude Kelvin waves that was reported in Refs. [60,61]. Indeed, Kelvin waves are clearly observed in 3D visualizations of vortex rings driven at finite temperatures by the TGPE as it is apparent in Fig. 12 [obtained in the same way that Fig. 9(b)].

Following Ref. [61], Kelvin waves of amplitude A and wavelength $2\pi R/N$ on a ring of radius R are parametrized, in cylindrical coordinates r, ϕ, and z, as

$$x = (R + A\cos N\phi)\cos\phi, \tag{82}$$

$$y = (R + A\cos N\phi)\sin\phi, \tag{83}$$

$$z = -A\sin\phi. \tag{84}$$

In the limit $N \gg 1$ the dispersion relation $\omega(k)$ of the Kelvin wave [Eqs. (82)–(84)] is given by [60]

$$\omega(k) = \frac{\hbar}{2m}k^2\left[\ln\left(\frac{8R}{\xi}\right) - a\right], \tag{85}$$

where $k = N/R$ and a is the core model-depending constant in formula (75).

The anomalous translational velocity caused by an excited Kelvin wave was first reported by Kiknadze and Mamaladze [60] in the framework of the local induction approximation (LIA). The effect was then obtained and numerically characterized within the Biot-Savart equation by Barenghi *et al.* [61]. The anomalous translational velocity v_a of a vortex ring reads (in the limit $N \gg 1$, see Eq. (26) of Ref. [60])

$$v_a \approx u_i\left(1 - \frac{A^2N^2}{R^2}\right), \tag{86}$$

where $u_i = V_{\rm ring}$ is the self-induced velocity (75) without Kelvin waves.

The variation of the energy of a vortex ring caused by a (small amplitude) Kelvin wave can be estimated as

$$\Delta E = \frac{dH_{\rm ring}}{dR}\frac{\Delta L}{2\pi}, \tag{87}$$

where $H_{\rm ring}$ is the energy given by Eq. (77) and the length variation ΔL produced by the Kelvin wave [Eqs. (82)–(84)] is given, at lowest order in the amplitude A/R, by $\Delta L = \pi A^2N^2/R$. Assuming equipartition of the energy of Kelvin waves with the heat bath implies $\Delta E = k_BT$, which yields the value of A^2N^2/R^2 as function of T:

$$\frac{A^2N^2}{R^2} = \frac{m^2k_BT}{\pi^2\rho_\infty\hbar^2R\left(\log\frac{8R}{\xi} - a\right)}. \tag{88}$$

The equipartition law (88) can also be directly obtained as the classical limit of the quantum distribution computed by Bareghi *et al.* [62], up to a redefinition of the core constant model a [see Eq. (25) in Ref. [62]]. Let us remark at this point that, at low temperature and in nonequilibrium conditions, the presence of a Kelvin wave cascade at scales between the intervortex distance and ξ (see Refs. [63,64]) can lead to a different dependence of the amplitude on the wave number.

We finally assume that the slowing-down effect of each individual Kelvin wave is additive and that the waves populate all the possible modes. Kelvin waves are bending oscillations of the quantized vortex lines, with wave number $k \lesssim 2\pi/\xi$. The total number of modes can thus be estimated as

$$\mathcal{N}_{\rm Kelvin} \approx 2\pi R/\xi. \tag{89}$$

Replacing A^2N^2/R^2 in Eq. (86) by Eq. (88) and multiplying by the total number of waves $\mathcal{N}_{\rm Kelvin}$ we obtain the following expression for the anomalous translational effect due to thermally exited Kelvin waves

$$\frac{\Delta v_L}{u_{\rm i}} \equiv \frac{u_{\rm i} - v_{\rm a}}{u_{\rm i}} \approx \frac{2k_BTm^2}{\pi\rho_\infty\xi\hbar^2}\frac{1}{\log\frac{8R}{\xi} - a}. \tag{90}$$

The temperature dependence of the equipartition estimate (90) of the thermal slowdown is plotted on Fig. 11(b) (top straight line). The data obtained form the measurements of the rings velocity in the TGPE runs is in very good agreement with the estimate (90).

As discussed in Refs. [3,13] the TGPE gives a good approximation to physical (quantum) Bose-Einstein condensate (BEC) only for the modes with high phonon occupation number. In this sprit quantum effects on the Kelvin waves oscillations must also be taken into account to obtain the total slowing-down effect in a BEC. The TGPE estimation (90)

can be adapted to weakly interacting BEC by the following considerations.

At very low temperatures, because of quantum effects, only a limited range of low-wave-number Kelvin waves are in equipartition. This range is determined by the relation $k \leqslant k_{\rm eq}$ with $\hbar\omega(k_{\rm eq}) = k_B T$ and the dispersion relation (85), it reads:

$$k_{\rm eq} = \sqrt{\frac{k_B T\, 2m}{\hbar^2\left[\ln\left(\frac{8R}{\xi}\right) - a\right]}} \tag{91}$$

and can also be expressed as

$$k_{\rm eq} = \sqrt{\frac{4\pi\, n^{2/3}}{\zeta\left(\frac{3}{2}\right)^{2/3}\left[\ln\left(\frac{8R}{\xi}\right) - a\right]}}\left(\frac{T}{T_\lambda}\right)^{1/2}. \tag{92}$$

where T_λ is the Bose-Einstein condensation temperature of noninteracting particles (68) and the relation between the interatomic distance ℓ and the vortex-core size ξ are given in Eq. (66).

Observe that $k_{\rm eq}$ varies from $k_{\rm eq} = 0$ at $T = 0$ to a wave number of order $k_{\rm eq} \sim \ell^{-1}$ at T_λ and is equal to $k_\xi = 2\pi/\xi$ at T^* defined by

$$T^* = 8\pi^2\zeta\left(\frac{3}{2}\right)^{2/3}\left[\ln\left(\frac{8R}{\xi}\right) - a\right]\left(\frac{\tilde a}{\ell}\right)T_\lambda. \tag{93}$$

Therefore, at temperatures $T^* < T < T_\lambda$, the energy of all Kelvin waves are in equipartition and equation (90) thus applies directly.

It is natural to suggest that an additional effect, caused by the quantum fluctuations of the amplitudes of Kelvin waves, will take place at low temperatures $T < T^*$. This quantum effect can be estimated by using the standard relation for the energy of the fundamental level of a harmonic oscillator $\Delta E = \hbar\omega(k)/2$. Applied to the Kelvin waves, this relation yields the k-independent quantum amplitude $A_Q^2 = m/4\pi^2 R\rho$. The quantum effect can thus be estimated as the sum

$$\sum_{N=\mathcal{N}_{\rm Kelvin}^{\rm eq}}^{\mathcal{N}_{\rm Kelvin}} \frac{A_Q^2 N^2}{R^2} \sim \frac{A_Q^2 {\mathcal{N}_{\rm Kelvin}}^3}{3R^2} = \frac{2m\pi}{3\rho\xi^3} = \frac{64\pi^{5/2}}{3\sqrt{2}}\left(\frac{\tilde a}{\ell}\right)^{3/2}. \tag{94}$$

The total effect is obtained superposing the thermal effect and the quantum effect and the final result is

$$\left.\frac{\Delta v_L}{u_i}\right|_{T<T^*} = \frac{64\pi^{5/2}}{3\sqrt{2}}\left(\frac{\tilde a}{\ell}\right)^{3/2} + \frac{(4/\sqrt{\pi})}{\zeta\left(\frac{3}{2}\right)C\left[\frac{R}{\xi}\right]^{3/2}}\left(\frac{T}{T_\lambda}\right)^{3/2} \tag{95}$$

$$\left.\frac{\Delta v_L}{u_i}\right|_{T>T^*} = \frac{8\sqrt{2\pi}}{\zeta\left(\frac{3}{2}\right)^{2/3}C\left[\frac{R}{\xi}\right]}\left(\frac{\tilde a}{\ell}\right)^{1/2}\frac{T}{T_\lambda}, \tag{96}$$

where $C[R/\xi] = \log\left(\frac{8R}{\xi}\right) - a$.

In the case of superfluid helium, where $\tilde a \sim \ell$, the GPE description is expected to give only qualitative predictions and, at best, order-of-magnitude estimates (see Ref. [4]). It is thus difficult to extend the above considerations, obtained in the case of weakly interacting BEC with $\tilde a \ll \ell$, to helium.

Nevertheless, the results obtained above in the weakly interacting case strongly suggest the presence of new slowing-down effects not included in the usual mutual friction descriptions of helium that predicts $\frac{\Delta v_L}{u_i} \sim \rho_n/\rho \sim (T/T_\lambda)^4$. The new effects, because of their temperature dependence [see Eq. (96)], should be dominant at low temperatures.

The zero-temperature quantum slowdown is independent of the ring diameter and the finite-temperature effects are stronger for small rings. Time-of-flight measurements of vortex rings in ^{4}He could be used to determine the translational velocity. The effect could also be studied in ultracold atomic gases BEC. For these systems the effect of the inhomogeneity of the superfluid should be taken into account [65].

VI. CONCLUSIONS

In summary, our main results were obtained by making use of a stochastically forced Ginzburg-Landau equation (SGLE) that permits us to efficiently obtain and control truncated Gross-Pitaevskii absolute equilibrium. This allowed us to show that the condensation transition observed in Refs. [13,27,28] corresponds to a standard second-order transition described by the $\lambda\phi^4$ theory.

We also found that thermodynamic equilibrium can be obtained by a direct energy cascade, in a way similar to that of Cichowlas *et al.* [21], accompanied by vortex annihilation as a prelude to final thermalization. Increasing the amount of dispersion of the system a slowdown of the energy transfer was produced inducing a partial thermalization independently of the truncation wave number. This new thermalization regime opens up an avenue to a further investigation of vortex dynamic in coflowing finite-temperature superfluid turbulence. In this context it would be interesting to study in the future, using a much higher resolution than in the present work, the dispersive bottleneck. In particular, to investigate the possibility of the coexistence of a well-established turbulent Kolmogorov cascade followed by a dispersive-induced partial-thermalization zone.

Using the SGLE in the presence of a counterflow we observed that the counterflow can block the contraction of vortex rings reported by Berloff and Youd [30] and also induce a dilatation. We directly measured the mutual friction coefficient related to the transverse force. An unexpected result was found by immersing a vortex ring in a finite-temperature bath: A strong dependence of the translational velocity in the temperature was observed. This effect was an order of magnitude above the transverse mutual friction effect. We explained this effect by relating it to to the anomalous translational velocity due to finite amplitude Kelvin waves that was previously found by Kiknadze and Mamaladze [60] and Barenghi *et al.* [61]. Assuming equipartition of the energy of the Kelvin waves with the heat bath yields a formula that gives a very good quantitative estimate of the numerically observed effect.

This new formula also gives an experimentally testable quantitative prediction for the thermal slowdown of vortex rings in weakly interacting Bose-Einstein condensates and superfluid ^{4}He. In this context, it would be interesting in the future to study (using a higher resolution than in the present work) the vortex dynamic of counterflowing finite-temperature superfluid turbulence. Note that, in the context of BEC (where experiments are performed within a confining potential) the wave function ψ must be expanded using another basis of

orthogonal independent functions than the Fourier modes (e.g., the eigenfunctions of the harmonic oscilator), see Ref. [66] where the apparent arbitrariness of the truncation parameter is also discussed. About this last point, also see the discussion around Eqs. (65) and (70) at the end of Sec. IV B of the present work about the upper limit $k_{\rm eq}$ of the equipartition range that follows from the quantization of phonons in a physical BEC.

The TGPE dynamics was thus found to contain many physically sound phenomena of finite-temperature superflows. This strongly suggests the possibility to obtain the propagation of second sound waves in the TGPE. Some preliminary results support this conjecture (data not shown); however, very high resolutions seem to be needed and this will be the subject of a future work.

ACKNOWLEDGMENTS

We acknowledge useful scientific discussions with G. Düring and S. Rica. The computations were carried out at IDRIS (CNRS).

APPENDIX A: CONSERVATION LAWS AND DEALIASING

In the standard incompressible Euler case, for quadratic nonlinearities and quadratic invariants, the system can be correctly dealiased using the 2/3 rule that consists in truncation for wave number $|\mathbf{k}| < k_{\rm max} = N/3$, where $N/2$ is the largest wave number of the discrete system. With this procedure, one-third of the available modes are not used. Such a discrete dealiased pseudospectral system exactly conserves the quadratic invariant and is therefore identical to the original Galerkin truncated system.

In the TGPE case, the problem is more complicated because the equation is cubic and the invariants are quartic. Let us first recall Parseval's theorem that states $\int d^3x f(\mathbf{x})g^*(\mathbf{x}) = V\sum_{\mathbf{k}} \hat{f}_{\mathbf{k}}\hat{g}^*_{\mathbf{k}}$, where $\hat{f}_{\mathbf{k}}$ and $\hat{g}_{\mathbf{k}}$ are the Fourier transform of f and g. This identity remains valid in truncated systems and it holds whether the functions are dealiased or not. The integration by parts formula is a consequence of Parseval's theorem:

$$\int d^3x\, f\frac{\partial g^*}{\partial x_j} = V\sum_{\mathbf{k}} -ik_j \hat{f}_{\mathbf{k}}\hat{g}^*_{\mathbf{k}} = -\int d^3x\,\frac{\partial f}{\partial x_j}g^*.$$

Remark that the product rule $(fg)' = f'g + fg'$ is only valid if the fields are dealiased.

The conservation of the total number of particles is directly obtained using the GPE (1)

$$\frac{dN}{dt} = \int d^3x(\dot{\psi}\bar{\psi} + \psi\dot{\bar{\psi}}) = \frac{i\hbar}{2m}\int d^3x(\bar{\psi}\nabla^2\psi - \psi\nabla^2\bar{\psi}) = 0,$$

where the last equality is a consequence of the Parseval identity and is thus true independently of dealiasing. Similar relations lead to the conservation of the energy H.

Using the dealiased TGPE (18) the conservation law for the momentum reads

$$\frac{dP_j}{dt} = 2g\int d^3x[(\partial_j\mathcal{P}_G[|\psi|^2])|\psi|^2 + \mathcal{P}_G[|\psi|^2]\partial_j|\psi|^2]. \tag{A1}$$

If ψ is dealiased, the 2/3 rule implies that

$$\int d^3x(\mathcal{P}_G[|\psi|^2]\bar{\psi})\partial_j\psi = \int d^3x\mathcal{P}_G[\mathcal{P}_G[|\psi|^2]\bar{\psi}]\partial_j\psi$$

$$\partial_j(\mathcal{P}_G[|\psi|^2]\bar{\psi}) = (\partial_j\mathcal{P}_G[|\psi|^2])\bar{\psi} + \mathcal{P}_G[|\psi|^2]\partial_j\bar{\psi}$$

$$\partial_j|\psi|^2 = \psi\partial_j\bar{\psi} + \partial_j\psi\bar{\psi},$$

it follows that $\frac{dP_j}{dt} = 0$. Without a Galerkin projector in Eq. (18) the aliased field would obey $(|\psi|^2\bar{\psi})\partial_j\psi + (|\psi|^2\psi)\partial_j\bar{\psi} \neq \partial_j(|\psi|^4)$ and the conservation of momentum would therefore be lost.

Conservation of N, H, and $\mathbf{P}$ can be numerically checked by using absolute equilibria with nonzero momentum. The conservation of $\mathbf{P}$ is ensured only if the system is dealiased. The error of aliased runs grow up to a 50% in a few units of time and is independent of the time step (data not shown). We thus believe that it would important to explicitly check the conservation of momentum when using finite-difference schemes, even if they exactly conserve the energy and the particle number.

APPENDIX B: LOW-TEMPERATURE CALCULATION OF THERMODYNAMIC FUNCTIONS

We are interested in computing the grand partition function $\mathcal{Z}$ in Eq. (47), where $F = H - \mu N - \mathbf{W}\cdot\mathbf{P}$ is written in terms of Fourier amplitudes as

$$\frac{H}{V} = \sum_{\mathbf{k}}\frac{\hbar^2k^2}{2m}|A_{\mathbf{k}}|^2 + \frac{g}{2}\sum A^*_{\mathbf{k}_3+\mathbf{k}_1}A_{\mathbf{k}_2}A^*_{\mathbf{k}_4+\mathbf{k}_2}\delta_{\mathbf{k}_3,-\mathbf{k}_4} \tag{B1}$$

$$N = V\sum_{\mathbf{k}}|A_{\mathbf{k}}|^2 \tag{B2}$$

$$P_j = \sum_{\mathbf{k}}\hbar k_j|A_{\mathbf{k}}|^2V, \tag{B3}$$

where $A_{\mathbf{k}} = 0$ if $k \geqslant k_{\rm max}$ and the second sum in H is over $\mathbf{k_1}$, $\mathbf{k_2}$, $\mathbf{k_3}$, $\mathbf{k_4}$.

The saddle point is determined by the condition $\frac{\partial F}{\partial A^*_{\mathbf{k}}} - \mu_0 A_{\mathbf{0}}V\delta_{\mathbf{k},\mathbf{0}} = 0$ that, separately written for $\mathbf{k} = \mathbf{0}$ and $\mathbf{k} \neq \mathbf{0}$, explicitly reads

$$(g|A_{\mathbf{0}}|^2 - \mu + \mu_0)A_{\mathbf{0}} + 2g\sum_{\mathbf{k_1}\neq\mathbf{0}}A_{\mathbf{0}}|A_{\mathbf{k_1}}|^2 + g\sum_{\mathbf{k_1},\mathbf{k_2}\neq\mathbf{0}}A_{\mathbf{k_1}}A^*_{\mathbf{k_2}-\mathbf{k_1}}A_{-\mathbf{k_2}} = 0 \tag{B4}$$

$$\frac{\hbar^2k^2}{2m}A_{\mathbf{k}} - \mu A_{\mathbf{k}} - \hbar\mathbf{W}\cdot\mathbf{k}\,A_{\mathbf{k}} + g\sum_{\mathbf{k_1},\mathbf{k_2}\neq 0}A_{\mathbf{k_1}}A^*_{\mathbf{k_2}+\mathbf{k_1}}A_{\mathbf{k}+\mathbf{k_2}} = 0 \tag{B5}$$

from which Eq. (48) follows.

To diagonalize $F = H - \mu N - \mathbf{W}\cdot\mathbf{P}$ we first apply the Bogoliubov transformation to $H - \mu N$ and then show that P is also diagonal in this basis. Replacing $B_{\mathbf{p}}$, defined by the transformation (52), in $H - \mu N$ (recall that $\mathbf{p} = \hbar\mathbf{k}$) and then imposing the diagonalization determines the coefficient L_p:

$$L_p = \frac{-2|A_{\mathbf{0}}|^2g - \frac{p^2}{2m} + \mu + \epsilon(p)}{|A_{\mathbf{0}}|^2g}, \tag{B6}$$

where $\epsilon(p)$ is given by

$$\epsilon(p) = \sqrt{\left(2|A_{\mathbf{0}}|^2 g + \frac{p^2}{2m} - \mu\right)^2 - |A_{\mathbf{0}}|^4 g^2}. \quad \text{(B7)}$$

The dispersion relation (54) is obtained by replacing $|A_{\mathbf{0}}|^2$ by its saddle-point value Eq. (48).

We now express $\mathbf{P}$ in the Bogoliubov base. Using (52) directly yields

$$|A_{\mathbf{p}}|^2 = |u_p|^2 |B_{\mathbf{p}}|^2 + |v_p|^2 |B_{-\mathbf{p}}|^2 + (u^*{}_p v^*{}_p B_{\mathbf{p}} B_{-\mathbf{p}} + \text{c.c.}). \quad \text{(B8)}$$

Replacing Eq. (B8) in the definition of $\mathbf{P}$ (B3), the last two terms vanish by symmetry and using the relation $|u_p|^2 - |v_p|^2 = 1$, the momentum (B3) reads $\mathbf{P} = \sum_{\mathbf{p}} \mathbf{p} |B_{\mathbf{p}}|^2 V$. Formula (53) is then finally obtained by gathering $H - \mu N$ and $\mathbf{W} \cdot \mathbf{P}$.

The mean value of the condensate amplitude is obtained as $V\overline{|A_{\mathbf{0}}|^2} = -\frac{\partial \Omega}{\partial \mu_0}|_{\mu_0=0}$. All the thermodynamic variables are directly generated by first putting $\mu_0 = 0$ in (59) and then by differentiation, using relation (32). The fluctuations of the number of particles are computed as $\overline{\delta N^2} = -\beta^{-1} \frac{\partial^2 \Omega}{\partial \mu^2}$. These quantities are explicitly listed below.

$$\begin{aligned}
\overline{|A_{\mathbf{0}}|^2} &= \frac{\mu}{g} - \frac{\mathcal{N}}{V\beta\mu} f_0\left[\frac{4m\mu}{P_{\max}^2}\right] \\
\bar{p} &= \frac{\mu^2}{2g} + \frac{\mathcal{N}}{V\beta}\left(\frac{2}{3} - f\left[\frac{4m\mu}{P_{\max}^2}\right] + \frac{2}{3}\frac{2w^2m^2}{P_{\max}^2} f'\left[\frac{4m\mu}{P_{\max}^2}\right]\right) \\
\bar{N} &= \frac{V\mu}{g} - \frac{\mathcal{N}}{\beta}\left(\frac{3}{2\mu} f\left[\frac{4m\mu}{P_{\max}^2}\right] - \frac{8w^2m^3}{P_{\max}^4} f_2\left[\frac{4m\mu}{P_{\max}^2}\right]\right)
\end{aligned}$$

$$S = \mathcal{N}\left(f\left[\frac{4m\mu}{P_{\max}^2}\right]\left(1 + \frac{2w^2m}{4\mu}\right) - \log\left[\frac{\beta\epsilon(P_{\max};\mu)}{e^{-\frac{5}{3}}}\right]\right)$$

$$\lambda_{\mathcal{N}} = \beta^{-1}\log\left[\beta\epsilon(P_{\max};\mu)\right] - \frac{1}{3\beta}\frac{2w^2m^2}{P_{\max}^2}\frac{1}{1+\frac{4m\mu}{P_{\max}^2}}$$

$$\bar{P}_z = \frac{\mathcal{N}}{\beta}\frac{wm}{\mu} f\left[\frac{4m\mu}{P_{\max}^2}\right] + \frac{3\mathcal{N}}{10\beta}\frac{w^3m^2}{\mu^2} f_1\left[\frac{4m\mu}{P_{\max}^2}\right]$$

$$\overline{\delta N^2} = \frac{V}{g\beta} + \frac{3\mathcal{N}}{4\beta^2\mu^2} f_1\left[\frac{4m\mu}{P_{\max}^2}\right], \quad \text{(B9)}$$

$$f[z] = z - z^{3/2}\cot^{-1}(\sqrt{z}) \quad \text{(B10)}$$

$$f_0[z] = 3(z + 3f[z])/4, \quad \text{(B11)}$$

$$f_1[z] = \frac{z}{z+1} - f(z), \quad \text{(B12)}$$

$$f_2[z] = \frac{d}{dz}(f[z]/z), \quad \text{(B13)}$$

The dependence of the entropy on the phase-space normalization constant is manifested by the presence of the logarithm term in S and $\lambda_{\mathcal{N}}$. Note that the function $S + \beta\lambda_{\mathcal{N}}$ is, however, completely defined. Also note that the pressure p must be computed, by definition, at constant total number of modes $\mathcal{N}$. All the thermodynamic relations discussed in Sec. II B can be explicitly checked on the low-temperature expressions. The previous formulas are represented as the solid lines that are confronted with the SGLE numerically generated data in Figs. 2(a) and 2(b).

[1] L. D. Landau and L. M. Lifshitz, *Course of Theoretical Physics: Fluid Mechanics*, 2nd ed. (Butterworth-Heinemann, Burlington, MA, 1987), Vol. VI.

[2] W. F. Vinen, Proc. R. Soc. London A **242**, 493 (1957).

[3] N. P. Proukakis and B. Jackson, J. Phys. B **41**, 203002 (2008).

[4] R. J. Donnelly, *Quantized Vortices in Helium II* (Cambridge University Press, Cambridge, UK, 1991).

[5] C. Nore, M. Abid, and M. E. Brachet, Phys. Rev. Lett. **78**, 3896 (1997).

[6] C. Nore, M. Abid, and M. E. Brachet, Phys. Fluids **9**, 2644 (1997).

[7] M. Kobayashi and M. Tsubota, Phys. Rev. Lett. **94**, 065302 (2005).

[8] J. Yepez, G. Vahala, L. Vahala, and M. Soe, Phys. Rev. Lett. **103**, 084501 (2009).

[9] M. Abid, M. E. Brachet, J. Maurer, C. Nore, and P. Tabeling, Eur. J. Mech. B-Fluid. **17**, 665 (1998).

[10] J. Maurer and P. Tabeling, Europhys. Lett. **43**, 29 (1998).

[11] G. P. Bewley, M. S. Paoletti, K. R. Sreenivasan, and D. P. Lathrop, Proc. Natl. Acad. Sci. USA **105**, 13707 (2008).

[12] M. S. Paoletti, M. E. Fisher, K. R. Sreenivasan, and D. P. Lathrop, Phys. Rev. Lett. **101**, 154501 (2008).

[13] M. J. Davis, S. A. Morgan, and K. Burnett, Phys. Rev. Lett. **87**, 160402 (2001).

[14] E. Zaremba, T. Nikuni, and A. Griffin, J. Low Temp. Phys. **116**, 277 (1999).

[15] B. Jackson, N. P. Proukakis, and C. F. Barenghi, Phys. Rev. A **75**, 051601 (2007).

[16] B. Jackson, N. P. Proukakis, C. F. Barenghi, and E. Zaremba, Phys. Rev. A **79**, 053615 (2009).

[17] T. D. Lee, Quart. J. Appl. Math. **10**, 69 (1952).

[18] R. H. Kraichnan, J. Acoust. Soc. Am. **27**, 438 (1955).

[19] R. H. Kraichnan, J. Fluid Mech. **59**, 745 (1973).

[20] S. A. Orszag, in *Fluid Dynamics, Proceedings of the 1973 Les Houches Summer School*, edited by R. Balian and P. L. Peube (Gordon and Breach, New York, 1977).

[21] C. Cichowlas, P. Bonaïti, F. Debbasch, and M. Brachet, Phys. Rev. Lett. **95**, 264502 (2005).

[22] W. J. T. Bos and J. P. Bertoglio, Phys. Fluids **18**, 071701 (2006).

[23] G. Krstulovic and M. Brachet, Physica D **237**, 2015 (2008).

[24] G. Krstulovic, P. D. Mininni, M. E. Brachet, and A. Pouquet, Phys. Rev. E **79**, 056304 (2009).

[25] U. Frisch, S. Kurien, R. Pandit, W. Pauls, S. S. Ray, A. Wirth, and J. Z. Zhu, Phys. Rev. Lett. **101**, 144501 (2008).

[26] G. Krstulovic, C. Cartes, M. Brachet, and E. Tirapegui, Int. J. Bifurcation Chaos. **19**, 3445 (2009).
[27] C. Connaughton, C. Josserand, A. Picozzi, Y. Pomeau, and S. Rica, Phys. Rev. Lett. **95**, 263901 (2005).
[28] A. Picozzi, G. Düring, and S. Rica, Physica D **238**, 1524 (2009).
[29] N. G. Berloff and B. V. Svistunov, Phys. Rev. A **66**, 013603 (2002).
[30] N. G. Berloff and A. J. Youd, Phys. Rev. Lett. **99**, 145301 (2007).
[31] J. Zinn-Justin, *Phase Transitions and Renormalisation Group* (Oxford University Press, New York, 2007).
[32] D. J. Amit and V. Martin-Mayor, *Field Theory; The Renormalization Group and Critical Phenomena* (World Scientific, Singapore, 2005).
[33] M. Abid, C. Huepe, S. Metens, C. Nore, C. T. Pham, L. S. Tuckerman, and M. Brachet, Fluid. Dyn. Res. **33**, 509 (2003).
[34] D. Gottlieb and S. A. Orszag, *Numerical Analysis of Spectral Methods* (Society for Industrial and Applied Mathematics, Philadelphia, 1977).
[35] L. D. Landau and L. M. Lifshitz, *Course of Theoretical Physics Statistical Physics (Part 1)* (Butterworth-Heinemann, Burlington, MA, 1996), Vol. V.
[36] N. G. van. Kampen, *Stochastic Processes in Physics and Chemistry* (North-Holland, New York, 1981).
[37] F. Langouche, D. Roekaerts, and E. Tirapegui, *Functional Integration and Semiclassical Expansions* (D. Reidel, Dordrecht, 1982).
[38] V. A. Zagrebnov and J. B. Bru, Phys. Rep. **350**, 292 (2001).
[39] J. Mathews and R. Lee Walker, *Mathematical Methods of Physics* (W. A. Benjamin, Amsterdam, 1970).
[40] E. M. Lifshitz and L. P. Pitaevskii, *Course of Theoretical Physics: Statistical Physics (Part 2)* (Butterworth-Heinemann, January 1980), Vol. IX.
[41] J. A. Lipa, J. A. Nissen, D. A. Stricker, D. R. Swanson, and T. C. P. Chui, Phys. Rev. B **68**, 174518 (2003).
[42] G. Krstulovic and M. Brachet, Phys. Rev. Lett. **105**, 129401 (2010).
[43] E. Fermi, J. Pasta and S. Ulam, LASL Report LA-1940, 1955.
[44] E. A. L. Henn, J. A. Seman, G. Roati, K. M. F. Magalhaes, and V. S. Bagnato, Phys. Rev. Lett. **103**, 045301 (2009).
[45] G. Krstulovic and M. Brachet, Phys. Rev. Lett. **106**, 115303 (2011).
[46] C. Huepe, S. Metens, G. Dewel, P. Borckmans, and M. E. Brachet, Phys. Rev. Lett. **82**, 1616 (1999).
[47] C. W. Gardiner, *Handbook of Stochastic Methods: For Physics, Chemistry and the Natural Sciences (Springer Series in Synergetics)* (Springer, Berlin, 1996).
[48] T. Winiecki, J. F. McCann, and C. S. Adams, Europhys. Lett. **48**, 475 (1999).
[49] C. Huepe and M. E. Brachet, Physica D **140**, 126 (2000).
[50] C. Huepe, L. S. Tuckerman, S. Métens, and M. E. Brachet, Phys. Rev. A **68**, 023609 (2003).
[51] C. T. Pham, C. Nore, and M. E. Brachet, Physica D **210**, 203 (2005).
[52] C. Nore, M. E. Brachet, E. Cerda, and E. Tirapegui, Phys. Rev. Lett. **72**, 2593 (1994).
[53] D. J. Thouless, P. Ao, and Q. Niu, Phys. Rev. Lett. **76**, 3758 (1996).
[54] G. E. Volovik, Phys. Rev. Lett. **77**, 4687 (1996).
[55] C. Wexler, Phys. Rev. Lett. **79**, 1321 (1997).
[56] H. E. Hall and J. R. Hook, Phys. Rev. Lett. **80**, 4356 (1998).
[57] E. B. Sonin, Phys. Rev. Lett. **81**, 4276 (1998).
[58] C. Wexler, D. J. Thouless, P. Ao, and Q. Niu, Phys. Rev. Lett. **80**, 4357 (1998).
[59] J. Fuchs *et al*., Phys. Rev. Lett. **81**, 4275 (1998).
[60] L. Kiknadze and Y. Mamaladze, J. Low Temp. Phys. **126**, 321 (2002).
[61] C. F. Barenghi, R. Hanninen, and M. Tsubota, Phys. Rev. E **74**, 046303 (2006).
[62] C. F. Barenghi, R. J. Donnelly, and W. F. Vinen, Phys. Fluids. **28**, 498 (1985).
[63] E. Kozik and B. Svistunov, Phys. Rev. Lett. **92**, 035301 (2004).
[64] V. S. L'vov and S. Nazarenko, JETP Lett. (Pis'ma v ZhETF) **91**, 464 (2010) (see: http://mi.mathnet.ru/eng/jetpl704).
[65] G. Krstulovic and M. Brachet, Phys. Rev. B **83**, 132506 (2011).
[66] P. B. Blakie and M. J. Davis, Phys. Rev. A **72**, 063608 (2005).